High Power Density Thermoelectric Generators with Skutterudites

Soufiane El Oualid, Iurii Kogut, Mohamed Benyahia, Eugen Geczi, Uwe Kruck, Francis Kosior, Philippe Masschelein, Christophe Candolfi, Anne Dauscher, Jan Dieter Koenig, et al.

High Power Density Thermoelectric Generators with Skutterudites

Soufiane El Oualid, Iurii Kogut, Mohamed Benyahia, Eugen Geczi, Uwe Kruck[†]*, Francis Kosior, Philippe Masschelein, Christophe Candolfi, Anne Dauscher, Jan Dieter Koenig, Alexandre Jacquot, Thierry Caillat, Eric Alleno, Bertrand Lenoir*[*]

[†] U. K. passed away in April 2020

Dr. S. El Oualid, Dr. I. Kogut, Dr. F. Kosior, Mr. P. Masschelein, Dr. C. Candolfi, Dr. A. Dauscher, Pr. B. Lenoir
Institut Jean Lamour, UMR 7198 CNRS – Université de Lorraine, Campus ARTEM, 2 allée André Guinier, BP 50840, 54011 Nancy, France
E-mail: bertrand.lenoir@univ-lorraine.fr

Mr. E. Geczi, Mr. U. Kruck, Pr. J. D. Koenig, Dr. A. Jacquot
Fraunhofer Institute for Physical Measurement Techniques IPM, 79110 Freiburg, Germany

Dr. M. Benyahia, Dr. E. Alleno
Univ Paris Est Creteil, CNRS, ICMPE, UMR 7182, 2 rue Henri Dunant, 94320 Thiais, France

Dr. T. Caillat
Jet Propulsion Laboratory, California Institute of Technology, Pasadena, CA 91109, USA

Keywords: Thermoelectric, thermoelectric modules, power generation, skutterudite

Thermoelectric generators (TEGs) offer a versatile solution to convert low-grade heat into useful electrical power. While reducing the length of the active thermoelectric legs provides an efficient strategy to increase the maximum output power density p_{max}, both the high electrical contact resistances and thermomechanical stresses are two central issues that have so far prevented a strong reduction in the volume of thermoelectric materials integrated. Here, we demonstrate how these barriers can be lifted by using a non-conventional architecture of the legs that consists in inserting thick metallic layers. Using skutterudites as a proof-of-principle, several single-couple and multi-couple TEGs with skutterudite layers of only 1 mm have been fabricated, yielding record p_{max} ranging from 3.4 up to 7.6 W cm^{-2} under temperature differences varying between 450 and 630 K. The highest p_{max} achieved corresponds to a sixtyfold increase per unit volume of skutterudites compared to 1-cm-long legs. Our work

establishes thick metallic layers as a robust strategy through which high-power-density TEGs may be developed.

1. Introduction

Thermoelectric materials have the ability to directly and reversibly convert a thermal gradient into electrical energy, offering an elegant and versatile way to recover energy from any heat source.[1-15] Thermoelectric generators (TEGs), consisting of *n*- and *p*-type legs composed of doped semiconductors, have been mostly used as reliable power supplies for rovers and deep-space probes.[10,11] Despite being an attractive solid-state technology primarily due to its high reliability and absence of greenhouse gas emissions, the limited use of TEGs in terrestrial applications is tied to their output performances, still surpassed by other green energy-conversion technologies such as solar cells.

The last decades have witnessed the emergence of novel families of thermoelectric materials such as skutterudites, half-Heusler or Zintl phases.[16-24] Their higher performances with respect to state-of-the art materials are captured through their dimensionless thermoelectric figure of merit $ZT = \alpha^2 T/\rho\kappa$ where α is the thermopower (or Seebeck coefficient), T is the absolute temperature, ρ is the electrical resistivity, κ is the total thermal conductivity, and α^2/ρ is the power factor.[10] Because increased ZT values yield enhanced conversion efficiency η,[10] these important advances have stimulated the development of TEGs operating at moderate temperatures (500 – 800 K). Several designs, including segmented legs composed of two or three joint thermoelectric materials,[10] have been investigated yielding very encouraging results with η values exceeding 10 %.[8,25,26] While the optimization of η is of prime importance for applications for which the heat source is limited or expensive, numerous waste-heat energy recovery applications do not require high TEG's efficiency due to the availability of unlimited, cost-free heat sources. The ability to generate the electrical power required to energize

autonomous electronic devices is then the primary concern, making the maximum output power $P_{max} = Ap_{max}$ (where A is the cross section area) the key parameter to be optimized.[10,27,28]

One of the most direct ways to increase P_{max} is to optimize the geometry of the *n*- and *p*-type legs, as highlighted by its simplest form determined for a fixed temperature difference ΔT, a matching of the electrical impedance and assuming temperature-independent transport properties of the thermoelectric materials[10,29-33]

$$P_{max} = \frac{(\alpha_p - \alpha_n)^2 \Delta T^2}{4R} = \frac{A(\alpha_p - \alpha_n)^2 \Delta T^2}{4L(\rho_n + \rho_p)} \quad (1)$$

where α_i and ρ_i are the thermopower and electrical resistivity of the leg $i = n, p$, respectively, and $R = \frac{L(\rho_n+\rho_p)}{A}$ is the internal resistance of the thermocouple L being the length of the *n*- and *p*-type legs. In addition to *n*- and *p*-type materials possessing high power factors, Eq.(1) shows that high P_{max} can be achieved by considering large surface areas A of the thermoelectric legs. However, the volume of thermoelectric materials scales with A, thereby rapidly increasing the cost per Watt generated. For this reason, lowering the length L seems to provide a straightforward strategy to enhance P_{max} and, meanwhile, reach cost-efficiency.

However, while seemingly simple, this strategy faces two major adverse effects, the control of which is then pivotal in achieving high P_{max}. The first effect is tied to the contribution of the electrical contact resistances ρ_c to the internal resistance of the legs, which is of increasing importance as L decreases. This effect limits P_{max} due to the resistance term R_c in the total internal resistance R_{int}, $R_{int} = R + R_c = \frac{L(\rho_n+\rho_p)}{A} + \frac{4\rho_c}{A}$ (assuming that the contact resistances are the same for the *n*- and *p*-type legs), which is no longer negligible.[31] Meanwhile, lowering L results in a significant increase in the thermal gradient undergone by the thermoelectric materials, which generate high thermomechanical stress levels. Because thermoelectric materials are often mechanically fragile, this effect strongly limits the robustness

of the legs and hence, the lifetime of the module. Moreover, a strong reduction in L tends to detrimentally impact the conversion efficiency η through a decrease in ΔT due to the interfacial thermal resistance (see Supporting Information),[29-33] thus placing a lower bound below which this strategy will no longer be viable. Due to these difficulties, only few studies have so far attempted to exploit this strategy to optimize P_{max}, if we except the specific case of μ-TEGs that integrate thin films with L on the order of tens of μm or less.[34-42] While μ-TEGs are currently being extensively investigated as a possible solution to power Internet-of-things autonomous devices such as wireless sensors or networking devices,[34,40,41] they only operate around room temperature with limited P_{max} ranging from μW to mW. Both increasing this level of power and enlarging their operating temperature are of particular interest and would open up new avenues to harvest low-grade heat in many industrial sectors (ovens, steam lines, hot fluid, motors, heating…) or in domestic devices (cookers, stoves…), thereby widening the application landscape of TEGs.

Here, leveraging on prior achievements on the development of TEGs,[29-33] we demonstrate how these two issues can be successfully overcome using a non-conventional design of the thermoelectric legs that enables to reduce the length of the active thermoelectric layers to only 1 mm while concomitantly maintaining both η and electrical contact resistances to state-of-the-art values.[14,15,43-56] The key design principle consists in inserting a thick layer of metallic composites, acting as a buffer, between the active thermoelectric materials sandwiched by the diffusion barrier and the metallic interconnections or electrodes. Among their advantages, these composites enable limiting the thermomechanical stresses undergone by the thermoelectric materials and easing the final brazing of the legs on the metallic interconnections. As a proof of principle, we used as thermoelectric materials *n*- and *p*-type skutterudites of chemical compositions $In_xCo_4Sb_{12}$ ($0.16 \leq x \leq 0.20$) and $Ce_{0.90}Fe_3CoSb_{12}$, respectively, in order to take full advantage of the good understanding of their chemistry

acquired over the last two decades and their high power factors.[10,16-18] The robustness and versatility of our approach is demonstrated by the fabrication of several single- and multi-couples TEGs with two distinct diffusion barriers (Ti or Ni) and compositions of the metallic composites (Ti/Cu or Ti/Ag), showing that both types of layers can be easily adapted to the integrated thermoelectric material. With conversion efficiencies ranging between 6.5 and 6.9% that are comparable to state-of-the-art values for non-segmented skutterudite legs,[14,15,43-56] the measured output power density p_{max}, varying from 3.4 up to 7.6 W cm^{-2} for applied ΔT between 450 and 630 K, are the highest achieved so far for skutterudite-based TEGs.

2. Results and Discussion

2.1 Design and fabrication of the thermoelectric legs

The non-conventional design of the *n*- and *p*-type thermoelectric legs consists in (Ti/Cu)$_{n,p}$ metallic composites placed on either side of the active skutterudites (**Figure 1**). A pure Ti layer of 25 µm is inserted between the skutterudites and the (Ti/Cu)$_{n,p}$ composites that serves as a diffusion barrier, preventing diffusion of the skutterudite elements towards the metallic composites or Cu contacts at high temperatures. A central aspect of the assembly of both legs is the applied thermomechanical cycle using the spark plasma sintering (SPS) technique, which allows for the consolidation of the assembly (metallic composite/diffusion barrier/skutterudite/diffusion barrier/metallic composite) in one single step (Figure S1 in Supporting Information). Furthermore, the temperature-pressure cycle has been carefully optimized for each type of leg to achieve flat interfaces between the different layers and good electrical contacts (see below). Importantly, changing the nature or chemical composition of one of the three layers requires a re-optimization of the SPS cycle.

The key role played by these 1-mm-thick metallic composites is demonstrated by their ability to limit the thermomechanical stresses undergone by the skutterudites due to the differences between the thermal expansion coefficients α_T of the skutterudites ($\alpha_T \sim 9.3\times10^{-6}$ K^{-1} and 11.3×10^{-6} K^{-1} at 300 K for the *n*- and *p*-type skutterudites, respectively) and those of the lower and upper metallic contacts made of Cu ($\alpha_T \sim 16.5\times10^{-6}$ K^{-1} at 300 K) that is usually used to connect the thermoelectric legs. The $\alpha_T(T)$ curves of the *n*- and *p*-type skutterudites measured up to 773 K, shown in **Figure 2**, evidence a nearly-linear behavior above 423 K with increasing temperature, reaching 12.5×10^{-6} K^{-1} and 15.0×10^{-6} K^{-1} at 773 K for the *n*- and *p*-type skutterudites, respectively. Because of the mismatch in α_T between the *n*- and *p*-type skutterudites,[57] the chemical composition of the metallic composite has been specifically adapted and hence, differs between the *n*- and *p*-type legs. Due to the large difference in the α_T value of elemental Ti and Cu (8.5×10^{-6} K^{-1} and 16.0×10^{-6} K^{-1} at 300 K, respectively), the α_T values can be accommodated by adjusting the Ti-to-Cu volume ratio according to the Reuss model[58]

$$\alpha_T^{skutterudite} = \alpha_T^{composite} = x\alpha_T^{Cu} + (1-x)\alpha_T^{Ti}$$

where x is the volume fraction of Cu. From the above-mentioned values of α_T, volume fractions of $x = 0.37$ and $x = 0.10$ were used for the *p*- and *n*-type legs, respectively. The pertinence of this simple approach is confirmed by the $\alpha_T(T)$ data measured on each metallic composite (see Figure 2), which demonstrates that the α_T values are close to those of the respective skutterudites up to 523 K. A difference between both values is solely observed for the *p*-type skutterudite at higher temperatures, being at most 10% at 773 K. Of note, other combinations of elements used in prior studies on skutterudite-based TEGs may be also considered such as Mo/Cu or Al/Ti for instance.[31] As a further demonstration of the versatility

of the present approach, a detailed characterization of *n*- and *p*-type thermoelectric legs with $(Ti/Ag)_{n,p}$ composites and Ni acting as the diffusion barrier are provided in the Supporting Information (Figures S2 to S9 in Supporting Information). Although the significant diffusion of Ni towards the skutterudites will prevent its use due to the induced rapid deterioration of the thermoelectric performances of the TEG, the large phase space for the choice of the nature of these two layers is of particular importance for determining the most suitable combinations of elements to achieve long-term stability, as recently demonstrated in skutterudite-based TEGs with Nb as the diffusion barrier.[15] The results obtained herein show that the chemical composition of the composites and the diffusion barrier may be adapted to the thermoelectric materials on a case-by-case basis.

The beneficial role of these metallic composites on the mechanical stability of the TEGs is supported by three-dimensional finite-element analyses of the distribution of the equivalent Von-Mises stresses, calculated for a single couple with an illustrative temperature difference ΔT of 500 K and for skutterudite length L varying between 1 and 3 mm (**Figure 3**). The boundary conditions used in these calculations are described in the Supporting Information. In the absence of metallic composites (Figure 3a), the thermal expansion of the skutterudites, when subjected to high temperature differences, induces the development of tensile stresses, the level of which increases with decreasing L due to the corresponding increase in the thermal gradient. Upon decreasing L from 3 to only 1 mm, the maximum tensile stress level undergone by the skutterudites may exceed their tensile strength (see Supporting Information), resulting in the breakage of the legs. Because of differences in α_T between the *n*- and *p*-type skutterudites, this limit is first reached in the latter. In contrast, the addition of the metallic composites on either side of the skutterudites maintains the maximum tensile stress in the skutterudites to values well below their tensile strength down to $L = 1$ mm (Figure 3b). Of note, this beneficial effect does not originate from a decrease in the ΔT undergone by the skutterudites due to the additional

thermal resistance induced by the composites (see below). Additional calculations performed on this assembly with an increased ΔT yielding a temperature difference of 500 K across the skutterudites confirm that the maximum stress level reached still remains well below their tensile strength (see Table S1 in Supporting Information). The positive effect of these metallic composites on the mechanical properties of the legs can be qualitatively understood by taking into account their specific mechanical characteristics. In the elastic regime (that is, under low strain), their Young's moduli are lower than those of the skutterudites (see Table S1), which helps to decrease the overall rigidity of the legs. Furthermore, their plastic regime, characterized by a more or less flat plastic strain rate, is also beneficial to decrease the stress level undergone by the skutterudites at higher strain levels. For these reasons, the metallic composites can be considered as acting as buffers from a mechanical point of view. These results demonstrate that the integrity of the skutterudite layers and hence, the mechanical robustness of the TEG, can be maintained while decreasing the thickness of the skutterudite layer. Furthermore, increasing the number of couples will increase the total surface area of the legs and hence, will contribute to further reduction of the developed tensile stresses.

2.2 Characterization of the thermoelectric legs and interfaces

Scanning electron microscopy (SEM) images combined with energy dispersive X-ray spectroscopy (EDS) elemental mapping were performed to assess the spatial distribution of the elements and determine the nature of the interfacial reaction layer between the skutterudite and the diffusion barrier for both the *n*- and *p*-type legs (**Figure 4**). A central aspect evidenced by these analyses is the absence of porosity and cracks in the skutterudite layers and the presence of an interfacial reaction layer between the skutterudites and the metallic composites that plays a key role in determining the electrical contact resistance of the legs.

The microstructure of the Ti/Cu composites is characterized by an overall two-phase mixture of homogeneously-distributed Cu and Ti regions of variable sizes spanning a range from few μm up to about 100 μm. The higher density of Cu regions observed in the *p*-type leg compared to the *n*-type leg naturally reflects the different Cu-to-Ti volume ratios considered. In agreement with the Cu-Ti binary phase diagram,[59] the EDS maps further show the formation of several Cu-Ti compounds at the interfaces between the Cu and Ti regions giving rise to a thin layer of approximately 2 μm.

A closer inspection of the skutterudite/diffusion barrier interfaces shows that chemical reactions occurred during the consolidation process, giving rise to the presence of additional phases. These phases are confined to a layer of approximately 6 μm located along the interface between the Ti diffusion barrier and the skutterudite (see Figure 4). For the *n*-type leg, chemical analyses further reveal the development of $SbTi_2$ at the Ti interface followed by $TiSb_2$ and CoTiSb. Another very thin layer of an In-rich phase is also observed, which may correspond to the formation of indium oxide. For the *p*-type leg, similar analyses evidence the presence of a thin layer of approximately 6 μm that originates from the reaction between Ti and the skutterudite. The additional phases formed are also Ti-Sb alloys as well as a Fe-containing ternary phase. EDS maps further show that the Ti diffusion barrier enables preventing a strong diffusion of the skutterudite elements, notably Fe and Sb. Overall, in agreement with prior studies, these results show that Ti possesses several advantages that notably include a high reaction activity during the consolidation process that ensures the formation of interfacial layers consisting in electrically- and thermally-conductive Ti-based alloys and hence, a good bonding strength between the skutterudites and the metallic composites.

The quality of the electrical contact resistance achieved for both legs can be appreciated by considering the evolution of the resistance R measured at 300 K over the length of the legs x (**Figure 5**). Both $R(x)$ profiles are characteristic of low electrical contact resistance ρ_c

(Figure S10 in Supporting Information). The ρ_c values are as low as 0.57 and 3.0 μΩ cm^2 at the top and bottom interfaces, respectively, between the thick metallic layer and the *p*-type skutterudite, and 8.7 and 9.9 μΩ cm^2 for the *n*-type skutterudite. The values measured for the *n*-type skutterudite compare very well with those reported in the literature and, in the case of the *p*-type skutterudite, are among the lowest achieved so far.[14,15,43-56] The room-temperature ρ values of the skutterudites, inferred from the slope of the $R(x)$ curves, are in very good agreement with those measured on those materials separately (Figures S11, S12 and S13 in Supporting Information). These results show that the possible detrimental influence of the increased number of interfaces on the electrical contact resistances has been successfully minimized through a careful optimization of the applied SPS cycle, yielding excellent electrical joints between the skutterudites and the metallic composites.

As a final step of the fabrication process of the TEGs, the *n*- and *p*-type legs were brazed on AlN or Al_2O_3 ceramic plates (see Supporting Information file), onto which nickel-copper paths of 0.30 mm in thickness were pre-deposited. This step is particularly critical due to the necessity to induce a strong bonding between the semiconducting thermoelectric materials and the metallic interconnections in order to minimize the electrical contact resistances at their interface. However, the difficulty in brazing metals to semiconductors, or more generally to ceramics, is notably due to the insufficient wettability of most braze alloys on ceramics. In such a case, residual stresses often accumulate within the brazing layer once the process is completed, resulting in poor mechanical properties. For these reasons, the braze should possess a good wettability. In the present case, this issue is naturally overcome due to the metallic nature of the $(Ti/Cu)_{n,p}$ composites that facilitates the brazing process. The excellent wettability of the In-Cu-Ag braze (InCuSil) used herein is evidenced by SEM images (**Figure 6**), showing an interlayer structure Cu/braze/$(Ti/Cu)_{n,p}$ that spreads over a distance of about 20 μm. The resulting structure is typical of the eutectic Ag-Cu-In with an Ag-rich phase into which both In

and Cu have dissolved (light grey areas) coexisting with a Cu-rich phase containing dissolved In and Ag (dark grey areas). Intermetallic phases as well as reaction layers at the submicron scale are also observed at the interfaces braze/Cu and braze/$(Ti/Cu)_{n,p}$. Near this last interface, a reaction layer of $CuTi_2$ of about 1 µm in thickness is clearly visible. The elemental X-ray maps further reveal the diffusion of In in Cu over a distance of about 10 µm, both towards the Cu interconnection and the metallic composite, and the presence of Ti in the brazing layer.

2.3 Thermoelectric performances of the TEGs

In order to demonstrate the reproducibility and robustness of the present approach, both single- and multi-couple TEGs with length of the skutterudite layers varying between 0.5 and 3 mm have been fabricated and tested (**Figure 7**a). The shortening of the active skutterudite layers and the excellent control of the interfaces achieved concur to yield a P_{max} of 2.8 W cm^{-2} under a temperature difference ΔT of 450 K for a TEG consisting of one couple with 3-mm-length skutterudite layers. Further lowering the length of the skutterudite layers to only 1 mm in a four-couple TEG increases p_{max} to 3.3 W cm^{-2} for a similar temperature difference (Figure 7b). These performances, obtained using $(Ti/Cu)_{n,p}$ composites, have been further increased in a six-couple TEG with $(Ti/Ag)_{n,p}$ composites yielding 4.6 W cm^{-2} that increases to 7.6 W cm^{-2} under a ΔT of 630 K. The optimized geometry and technological choices made for the design of the legs concur to yield p_{max} values that surpass those achieved so far for skutterudite-based TEGs with a p_{max} of 2.1 W cm^{-2} under a ΔT of 580 K obtained with skutterudite layers of 4 mm (Figure 7c).[14,15,43-56] Equivalently, the highest P_{max} achieved corresponds to a sixtyfold increase in the output power generated per unit volume of skutterudites, a prominent aspect to reach cost-efficiency (Figure 7d). These significantly higher values stem from the strong reduction of the leg length while maintaining the internal electrical resistance of the module

R_{int} to low values, despite the presence of additional interfaces induced by the metallic composites. This last point further highlights the very good bonding achieved between the metallic composites and the skutterudites. The significant lowering of L down to 1 mm represents a nearly fourfold increase in p_{max} compared to that expected for conventional, one-centimeter-long legs (Figure 7e).

Measurements performed over several heating/cooling cycles (Figure S14 in Supporting Information) did not evidence any evident degradation of the output performances, indicative of the good mechanical stability of the 1-mm-length legs. Of particular relevance, this significant increase in p_{max} is not realized at the expense of the conversion efficiency η, which remains to appreciable experimental values ranging between 6.5 and 6.9% (Figure 7f), comparing very well with those reported for non-segmented skutterudite-based TEGs.[14,15,43-56] This result shows that the addition of thick metallic layers is a viable strategy to enhance the generated p_{max} at nearly η. While the primary goal of this study was to increase p_{max}, these results further evidence that this approach may be also beneficial for applications that necessitate high η, which may be then increased by using thermoelectric materials with higher *ZT* values than those of the present skutterudites.[14,15,16-24] All these experimental values match with the theoretical predictions of three-dimensional finite-element analyses (see Figure 7f and SI for details of the simulations), confirming the excellent control of the different steps of the fabrication process.

Additional results obtained on a TEG integrating 0.5 mm-thick skutterudite layers show that further lowering the length below 1 mm is detrimental to p_{max}, which contrasts with the predictions of Eq.(1) that does not take into account parasitic effects due to additional interfaces inevitably present in real devices. While the experimental p_{max} of 4.2 W cm^{-2} closely follows the theoretical predictions and remains well beyond the state-of-the-art values (see Figure 7c),[14,15,43-56] the lower p_{max} achieved with a length of the legs of 0.5 mm reflects the increasing

importance of thermal interface resistances at the interfaces, limiting p_{max} below the optimum skutterudite length of 1 mm.

The modelling of the overall output performances of the TEGs by three-dimensional finite-element analyses provides relevant insights into possible routes to further improving p_{max}. These calculations indicate that the active skutterudite layers are only subjected to around one half of the temperature difference applied on the module (**Figure 8**), due to the inevitable external contact thermal impedance between the TEG and the hot and cold reservoirs, and the thermal resistance induced by the $(Ti/Cu)_{n,p}$ metallic composite and the ceramics. The influence of these layers on the temperature drops is further highlighted by calculations performed on TEGs with $(Ti/Ag)_{n,p}$ metallic composites for 1-mm-long and 0.5-mm-long skutterudite layers (see Figure S9 in Supporting Information). Increasing the thermal conductivity of these two components or reducing their thicknesses are two possible strategies that would increase the temperature difference applied on the skutterudites and hence, the maximum output power delivered by the TEG. However, the optimum height of the metallic composites should correspond to a compromise between the temperature drop and the maximum thermomechanical stress level undergone by the skutterudites. Finally, because the thermoelectric properties of the *n*- and *p*-type skutterudites used herein correspond to state-of-the-art values,[16-18] further increasing their power factors by manipulating their chemical compositions would also contribute to further enhancement of p_{max}.[16-18,60-64]

Beyond these possibilities of further enhancement and the record values obtained for the highest ΔT applied, it is important to note that the p_{max} values of the present TEGs still remain higher than those reported in the literature when considering lower ΔT. This can be appreciated in both Figures 7b and 7c where the results obtained on a TEG with skutterudite layers of 1 mm (brown square symbols) with an applied ΔT of 350 K are reported. The measured p_{max} of 2.2 W cm^{-2} is higher than the best results reported so far for ΔT of at least 550 K. The possibility

to achieve high power densities despite the application of lower temperature difference is an appealing characteristic in terms of practicality and lifetime in real applications. In particular, applying lower ΔT values will significantly mitigate the sublimation of elements and the possible detrimental influence of interfacial phenomena over time, such as the growth of intermetallic layers due to the interdiffusion of elements or of the intermetallic compounds formed within the metallic composite layers. Meanwhile, lower ΔT values will be also beneficial to drastically decrease the thermomechanical stresses undergone by the skutterudites, further ensuring the mechanical robustness of the modules. Future detailed studies dedicated to the evolution of the interfacial phenomena and output performances over long-time periods will be important to determine the maximum operating temperature that can be safely undergone by these TEGs. Finally, achieving high power densities for relatively low ΔT thanks to the present architecture makes these modules the counterparts of high-cooling-capacity Peltier coolers using thin (< 1 mm) Bi_2Te_3-based materials and hence, pave the way towards a new landscape for TE power generation.

3. Conclusion

We have successfully developed a robust strategy to reach high output power densities with TEGs, while strongly limiting the volume of the integrated thermoelectric materials, by means of the addition of thick metallic layers in the thermoelectric legs. As a proof-of-principle demonstration of this approach, several single- and multi-couple TEGs with skutterudites as the active thermoelectric materials have been fabricated. These TEGs are able to deliver output power densities of up to 3.4 and 7.6 W cm^{-2} under temperature differences of 450 and 630 K, respectively, which significantly surpass the values achieved so far for skutterudite-based TEGs. The advantages of this non-conventional design of the thermoelectric legs are manifold. First, the thick metallic layers act as absorbers of the thermomechanical stresses induced by the

mismatch in the thermal expansion coefficients between the skutterudites and the metallic contacts, and thus, reduce the stresses undergone by the mechanically-fragile skutterudites. Second, they ease the final, yet critical, brazing step of the legs onto the Cu-pre-deposited ceramic plates. Third, their presence helps to avoid the overflow of the braze on the thermoelectric elements due to their small length, which would induce an electrical short-circuit. Fourth, they enable achieving high power densities even for relatively low temperature differences, a key characteristic to mitigate various temperature-induced effects detrimental to the output performances over time. The versatility of our approach is demonstrated by the use of two distinct compositions of the metallic composites (Ti/Cu and Ti/Ag) and diffusion barrier (Ti and Ni), both leading to similar thermoelectric performances. These experimental results, in excellent agreement with the predictions of three-dimensional finite-element analyses, show that our approach should be equally applicable to diverse highly-efficient thermoelectric materials, thus enabling the development of cost-efficient, miniaturized TEGs with high p_{max} that fill the gap between bulk and μ-TEGs. Further studies on the protection of these skutterudite-based high-power-density TEGs against oxidation as well as long-term stability tests are the necessary next steps to bring them closer to real applications.

4. Experimental Section

Synthesis and characterizations of the skutterudites: Polycrystalline samples of skutterudites of nominal compositions $In_xCo_4Sb_{12}$ with $0.16 \leq x \leq 0.20$ (*n*-type) and $Ce_yFe_3CoSb_{12}$ with $0.75 \leq y \leq 0.90$ (*p*-type) were prepared from high-purity elements. The *n*-type skutterudites were synthesized by direct reaction of the elements in evacuated-, carbon-coated-sealed silica tubes. The tubes were heated in a vertical furnace to 650°C, dwelt at this temperature for 96 h before being quenched in room-temperature water. The chemical homogeneity of the obtained pellets was improved by annealing them at 650°C for 96 h followed by a final quenching. For the *p*-

type composition, Ce, Fe and Co were first melted in an induction furnace. The ingot was crushed in an agate mortar and the resulting coarse-ground powders were reacted with Sb in a sealed, carbon-coated silica tube placed in a rocking furnace at 650°C for 96 h. The mixture was ground by ball-milling into fine powders which were further pelleted and annealed again at 650°C for 96 h. The annealed pellets were then ground into fine powders.

The crystal structure was verified by powder X-ray diffraction measurements and the lattice parameters, strongly sensitive to the In or Ce content, were determined from Rietveld refinements against the PXRD data using the FullProf software.[65] These analyses confirmed the successful insertion of In and Ce into the cages of the cubic crystal structure of skutterudites described in the $Im\bar{3}$ space group. The inferred lattice parameters are consistent with literature data and correspond to the expected values for nominal In and Ce contents of $0.16 \leq x \leq 0.20$ and $0.75 \leq y \leq 0.90$, respectively.

A part of the prepared powders was consolidated by spark plasma sintering (SPS, Dr Syntex 505) in order to assess their thermoelectric properties between 300 and 800 K. To this end, the powders were placed in a graphite die and consolidated at 620°C for 5 – 10 min. under a uniaxial pressure of 50 MPa. The geometrical density of the consolidated cylindrical pellet, determined from weight and dimensions of the pellets, was found to be higher than 97% of the theoretical density. The consolidated pellets were subsequently cut with a diamond-wire saw into samples of appropriate shape and size for high-temperature transport properties measurements.

Electrical and thermal transport measurements and dilatometry: Thermal diffusivity d measurements were performed between 300 and 800 K using a laser flash instrument (LFA 457, Netzsch) on cylindrical-shaped samples of 10 mm in diameter and around 1 mm in thickness. Prior to these measurements, both sides of the samples were spray-coated with a thin layer of graphite. The thermal conductivity was calculated according to the relation $\kappa = dC_p\rho_V$ where

C_p is the isobaric specific heat and ρ_V is the density. As a first approximation, C_p was calculated using the Dulong-Petit law and was thus considered as temperature-independent. The temperature dependence of the density has been neglected. Electrical resistivity and thermopower were measured in the same temperature range on bar-shaped samples of dimensions 2×2×8 mm^3 using a ZEM-3 instrument (Ulvac-Riko). The thermal expansion coefficient α_D of the *n*- and *p*-type skutterudites was determined from 300 up to 773 K on bar-shaped samples of dimensions 2.5×2.5×9 mm^3 using a dilatometer (DIL402, Netzsch). An alumina sample was used as a standard for these measurements.

Preparation of the n- and p-type thermoelectric legs: The thermoelectric legs were prepared by considering two possible approaches. In the first approach, the diffusion barrier and the metallic composites were placed on either side of dense cylindrical pellets of *n*- or *p*-type skutterudites, and subsequently consolidated by SPS. As a second approach, the assembly of the *n* and *p*-type legs has been realized by cold-pressing the different layers in the sequence $(Ti/Ag)_{n,p}$/Ni layer/(dense skutterudite)$_{n,p}$/Ni layer/$(Ti/Ag)_{n,p}$ or $(Ti/Cu)_{n,p}$/Ti layer/(powdered skutterudite)$_{n,p}$/Ti layer/$(Ti/Cu)_{n,p}$. The obtained structure was subsequently sintered within one single step using SPS. While both approaches led to similar results and thermoelectric performances of the final TEG, the second approach was found to improve reproducibility.

For both approaches, the Ni or Ti layers were cut from Ni or Ti foils of 25 μm in thickness into discs of 10 mm in diameter. Those disks were chemically washed in a hydrofluoric acid/nitric acid/water bath to remove any oxide layer. This chemical attack reduces the thickness of the discs by 15 to 20%. The Ti/Ag and Ti/Cu metallic composites were prepared by mechanically-mixing Ag or Cu powders (100 μm according to the supplier) with Ti powders (44 μm according to the supplier). The mixed powders were cold-pressed into cylindrical pellets of 10 mm in diameter under a uniaxial pressure of 130 MPa yielding a thickness of around 1 mm with a density corresponding to about 80% of the theoretical density. In order to

characterize their thermal and electrical properties, some pellets were consolidated by spark plasma sintering following the same cycle as that used for the preparation of the thermoelectric leg (see below) in order to acquire experimental data that correspond as close as possible to those of the final legs.

The thermal expansion coefficients of the $(Ti/Ag)_n$, $(Ti/Ag)_p$, $(Ti/Cu)_n$ and $(Ti/Cu)_p$ compositions were measured under the same experimental conditions used for the skutterudites. Similarly, the electrical resistivity, thermopower and thermal diffusivity were also measured.

Module fabrication and characterization: The consolidated sandwiches were polished and cut into rectangular-shaped bars of 1.5 or 4 mm in length (0.5 or 3 mm of skutterudite, respectively, and 1 mm of buffer layers) and 2×(2-2.5) mm^2 in surface area. All surfaces of the bars have been carefully polished to ensure their flatness and parallelism and to obtain similar heights of the legs. The electrical connection between the thermoelectric legs was realized using AlN or Al_2O_3 plates of 0.63 mm in thickness onto which nickel-copper paths of 0.30 mm in thickness were deposited (C-Components and Curamik). The surface area of these plates is around 1or 4 cm^2 depending on the size of the module. The thermoelectric legs were brazed on the Cu path using InCuSil or Al-Si based paste as the brazing alloy on home-made brazing setups.

The electrical contact resistance of the thermoelectric legs was measured at 300 K using a home-made set-up or a commercial set-up (Quick Home) which enables probing the resistance over the length of the legs with a resolution of 15 μm. Prior to measurements, gold was deposited on the faces of the polished legs.

The assembled TEGs with the $(Ti/Ag)_{n,p}$ and Ni layers were characterized in a home-made set-up, the details of which can be found in Ref. 50. Briefly, the test station consists of a vacuum chamber cooled by water that houses the cold and hot reservoirs, between which the thermoelectric module is inserted. The maximum temperature of the hot reservoir is 973 K while the temperature of the cold reservoir can vary between 288 and 373 K. A uniaxial pressing force and grafoil (0.36 mm in thickness) are used to minimize the external contact thermal

impedance between the module and the reservoirs. For each temperature difference applied on the module, the voltage-current characteristic curves were established by using a variable electrical load.

All the other TEGs composed of $(Ti/Cu)_{n,p}$ and Ti layers were characterized with a commercial Mini-PEM apparatus (Ulvac-Riko). The measurements were realized under primary vacuum (< 5×10^{-2} Pa) up to 773 K. The TEG is placed onto a copper platform connected to a spring. The platform is cooled by circulating water. The hot source is provided by a resistive heater placed on the top side of the TEG. Thanks to the presence of the spring, a pressure between 0.1 and 1 MPa can be applied on the TEG to ensure a better thermal coupling. In order to further improve the coupling on the hot and cold side of the TEG, a thin layer of papyex (thickness of 0.1 mm), covered with thermal grease, was placed on the top and bottom side of the TEG. The hot-side temperature was varied between 350 and 773 K while the cold-side temperature was maintained to about 300 K. Both temperatures were monitored using two thermocouples anchored on the respective surfaces of the TEG. The Mini-PEM allows to extract the output electrical power of the module through the voltage-current characteristic curves but also its efficiency by measuring the thermal power (Q_{out}, see next paragraph), which is dissipated at the cold side.

Three-dimensional finite-element analyses: Thermoelectric effects (Seebeck, Peltier and Thomson effects) are defined by the coupling of the heat ($\vec{q}$) and current density ($\vec{J}$) flows through a material. They can be modeled using the following coupled equations expressed, for an isotropic material, as[10,29,30]

$$\vec{q} = \pi\vec{J} - \kappa\vec{\nabla}T \quad (1)$$

$$\vec{J} = \sigma\vec{E} + \sigma\alpha\vec{\nabla}T \quad (2)$$

where $\vec{E}$ is the electric field that derives from the potential V ($\vec{E} = -\vec{\nabla}V$), $\vec{\nabla}T$ is the temperature gradient, π is the Peltier coefficient, κ is the total thermal conductivity, σ is the electrical conductivity and α is the thermopower (or Seebeck coefficient).

In a stationary state, the local energy balance and charge conservation can be expressed by the two equations[10,29,30]

$$\vec{\nabla}.\vec{q} = \vec{E}\vec{J} \tag{3}$$

$$\vec{\nabla}.\vec{J} = 0 \tag{4}$$

This set of partial differential equations, combined with Eq.(1) and Eq.(2), can be solved numerically by finite-element analyses to determine the temperature and electrical potential fields in the material. Herein, all the electrical and thermal characteristics of the modules were calculated using three-dimensional finite-element analyses implemented in the software COMSOL Multiphysics. The thermoelectric effects in steady state were expressed by the above-mentioned set of differential equations with temperature and electrical potential as unknown parameters. The three-dimensional distributions of these parameters, together with the electrical current density and heat flux, were solved using the boundary conditions of the experimental set-up (temperatures and thermal interface contact resistances) used to characterize the modules. These simulations were conducted on model thermoelectric modules of dimensions corresponding to the fabricated modules. The measured temperature dependences of the transport properties of the skutterudites and the Ti/Ag or Ti/Cu composites were fitted using third-order polynomials, which were used as input parameters in these calculations. The output power P reaches its maximum value P_{max} when the impedance matching condition is achieved, that is, when the electrical load matches the internal resistance

R_{int} of the module. The conversion efficiency η of the TEG was calculated using the following relation

$$\eta(I) = \frac{P(I)}{P(I) + Q_{out}(I)} \quad (5)$$

where the current I and output heat flow Q_{out} were calculated using $\vec{J}$ and $\vec{q}$, respectively.

The derivation of the stress-strain state in the modules was performed using the software COMSOL Multiphysics by considering the boundary conditions (thermal, electrical and mechanical) imposed by the Mini-Pem. For the mechanical aspects, a spring force at the bottom surface (initial pressure equal to 0.5 MPa), a free displacement of the AlN cold plate and a null displacement along the normal of the AlN hot side were applied. This load state was considered to be close to actual situations. Table S1 in Supporting Information gathers the mechanical and thermal properties of the materials constituting the module used in the modelling. The Young modulus and the tensile strength (in compression) of skutterudites were extracted from nano-indentation measurements. The Poisson ratio of the skutterudites and metallic composites were experimentally determined using sound velocity measurements at 300 K. The other parameters were taken from references mentioned in the Supporting Information. The Young's moduli and the yield strength of the metallic composites were averaged according to the Voigt law as a first approximation.[66] We assumed a brittle linear elastic behavior for the *n*- and *p*-type skutterudites and ceramic (AlN). An elastoplastic behavior was considered for the metallic composites and copper, for which the hardening is supposed to be linear. Moreover, the tensile strength of the skutterudites was considered to be the same as the tensile strength in compression. Moreover, except for the coefficient of thermal expansion (CTE) of skutterudites and composites, we further assumed, as a first approximation, that the other mechanical parameters are temperature independent. From all these data and assumptions, the equivalent

von-Mises tensile stresses were calculated in the modules made of a single couple of *n*- and *p*-type skutterudites.

Supporting Information

Supporting Information is available from the Wiley Online Library or from the author.

Author contributions

B. L., A. J., A. D., J. K., T. C. and E. A. supervised the project. M. B. prepared the *n*- and *p*-type skutterudite powders for (Ti/Cu) TEGs. P. M. and I. K. prepared the *n*- and *p*-type skutterudite powders, developed and synthesized the buffer materials, and optimized the densification process of the *n*- and *p*-type legs for the (Ti/Ag) TEG with active skutterudite layers of 0.5 mm. C. C. and B. L. performed the high-temperature transport property measurements on the various legs of the (Ti/Cu) and (Ti/Ag) modules. A. D. and S. O. carried out the SEM analyses of the different interfaces. S. O. and P. M. carried out the densification process of the *n*- and *p*-type legs for the (Ti/Cu) TEGs, characterized the legs, performed the brazing step and characterized the performances of the modules. S. O. and F. K. performed the three-dimensional finite-element analyses of the different modules. U. K. and E. G. carried out the densification process of the *n*- and *p*-type legs for the (Ti/Ag) TEG with active skutterudite layers of 1 mm. E. G. performed the measurements of the electrical contact resistances and assembled the (Ti/Ag) modules. E. G. and J. K. characterized the performances of the (Ti/Ag) modules. C. C. wrote the manuscript with inputs from all co-authors (except U. K.).

Acknowledgements

A. D. and A. J. acknowledge the financial support of the Agence Nationale de la Recherche (ANR) and the Deutsche Forschungsgemeinschaft (DFG) in the frame of the project WATTS ("Wafers-based thin thermoelectric systems development", ANR-11-PICF-0007). I. K.

acknowledges the financial support of the ANR in the frame of the WATTS project. E. A., A. D. and B. L. acknowledge the financial support of the Agence Nationale de la Recherche (ANR) in the frame of the project NANOSKUT ("Nanostructured skutterudites for thermoelectric generation", ANR-12-PRGE-0008). M. B. acknowledges the financial support of the ANR in the frame of the NANOSKUT project.

Received: ((will be filled in by the editorial staff))

Revised: ((will be filled in by the editorial staff))

Published online: ((will be filled in by the editorial staff))

Conflict of Interest

The authors declare no conflict of interest.

References

[1] L. E. Bell, *Science* **2008**, *321*, 1457.

[2] G. J. Snyder, E. S. Toberer, *Nature Mater.* **2008**, *7*, 105.

[3] D. Kraemer, Q. Jie, K. McEnaney, F. Cao, W. Liu, L. A. Weinstein, J. Loomis, Z. Ren, G. Chen, *Nat. Energy* **2016**, *1*, 16153.

[4] J. P. Heremans, M. S. Dresselhaus, L. E. Bell, D. T. Morelli, *Nat. Nanotechnol.* **2013**, *8*, 471.

[5] Y. Pei, X. Shi, A. LaLonde, H. Wang, L. Chen, G. J. Snyder, *Nature* **2011**, *473*, 66.

[6] X. Lu, D. T. Morelli, Y. Xia, F. Zhou, V. Ozolins, H. Chi, X. Zhou, C. Uher, *Adv. Energy Mater.* **2012**, *3*, 342.

[7] W.-D. Liu, D.-Z. Wang, Q. Liu, W. Zhou, Z. Shao, Z.-G. Chen, *Adv. Energy Mater.* **2020**, *10*, 2000367.

[8] J. Yu, Y. Xing, C. Hu, Z. Huang, Q. Qiu, C. Wang, K. Xia, Z. Wang, S. Bai, X. Zhao, L. Chen, T. Zhu, *Adv. Energy Mater.* **2020**, DOI: 10.1002/aenm.202000888.

[9] T. J. Slade, T. P. Bailey, J. A. Grovogui, X. Hua, X. Zhang, J. J. Kuo, I. Hadar, G. J. Snyder, C. Wolverton, V. P. Dravid, C. Uher, M. G. Kanatzidis, *Adv. Energy Mater.* **2019**, *9*, 1901377.

[10] D. M. Rowe, in *Thermoelectrics and its Energy Harvesting: Modules, Systems,* and *Applications in Thermoelectrics*, ed. D. M. Rowe, CRC Press, Boca Raton, **2012**.

[11] N. Jaziri, A. Boughamoura, J. Müller, B. Mezghani, F. Tounsi, M. Ismail, *Energy Rep.*, **2019**, DOI: 10.1016/j.egyr.2019.12.011.

[12] R. He, G. Schierning, K. Nielsch, K. *Adv. Mater. Technol.* **2018**, *3*, 1700256.

[13] F. Freer, A. V. Powell, *J. Mater. Chem. C* **2020**, *8*, 441.

[14] S. H. Park, Y. Jin, J. Cha, K. Hong, Y. Kim, H. Yoon, C.-Y. Yoo, I. Chung, *ACS Appl. Energy Mater.* **2018**, *1*, 1603.

[15] J. Chu, J. Huang, R. Liu, J. Liao, X. Xia, Q. Zhang, C. Wang, M. Gu, S. Bai, X. Shi, L. Chen, *Nat. Comm.* **2020**, *11*, 2723.

[16] B. C. Sales, D. Mandrus, R. K. Williams, *Science* **1996**, *272*, 1325.

[17] G. Rogl, P. Rogl, *Current Opinion in Green and Sustainable Chemistry* **2017**, *4*, 50.

[18] C. Uher in *Recent trends in thermoelectric materials research*, Vol. 69, Chap. 5, p. 139 – 253, Ed. T. M. Tritt, Academic Press, 2001.

[19] C. Fu, T. Zhu, Y. Pei, H. Xie, H. Wang, G. J. Snyder, Y. Liu, Y. Liu, X. Zhao, *Adv. Energy Mater.* **2014**, 1400600.

[20] S. Anand, K. Xia, T. Zhu, C. Wolverton, G. J. Snyder, *Adv. Energy Mater.* **2018**, 1801409.

[21] C. Fu, S. Bai, Y. Liu, Y. Tang, L. Chen, X. Zhao, T. Zhu, *Nat. Comm.* **2015**, ***6***, 8144.

[22] S. R. Brown, S. M. Kauzlarich, F. Gascoin, G. J. Snyder, *Chem. Mater.* **2006**, *18*, 1873.

[23] J. Zhang, L. Song, K. A. Borup, M. Ry Vogel Jorgensen, B. B. Iversen, *Adv. Energy Mater.* **2018**, 1702776.

[24] S. Ohno, U. Aydemir, M. Amsler, J.-H. Pöhls, S. Chanakian, A. Zevalkink, M. A. White, S. K. Bux, C. Wolverton, G. J. Snyder, *Adv. Funct. Mater.* **2017**, 1606361.

[25] A. Muto, J. Yiang, B. Poudel, Z. Ren, G. Chen, *Adv. Energy Mater.* **2013**, *3*, 245.

[26] M. Hong, K. Zheng, W. Lyv, M. Li, X. Qu, Q. Sun, S. Xu, J. Zou, Z.-G. Chen, *Energy Environ. Sci.* **2020**, *13*, 1856.

[27] S. LeBlanc, S. K. Yee, M. L. Scullin, C. Dames, *Renew. Sustain. Energy Rev.* **2014**, *32*, 313–327.

[28] G. Min, D. M. Rowe, J. Power Sources **1992**, *38*, 253.

[29] *Advanced thermoelectrics: materials, contacts, devices, and systems*, Eds Z. Ren, Y. Lan and Q. Zhang, CRC Press, 2017.

[30] R. R. Heikes, R. W. Ure, in *Thermoelectricity: Science and Engineering*, Interscience Publishers, New-York – London, 1961.

[31] Q. H. Zhang, X. Y. Huang, S. Q. Bai, X. Shi, C. Uher, L. D. Chen, *Adv. Eng. Mater.* **2016**, *18*, 194.

[32] D. Champier, *Energ. Convers. Manage.* **2017**, *140*, 167.

[33] D. K. Aswal, R. Basu, A. Singh, *Energ. Convers. Manage.* **2016**, *114*, 50.

[34] S. El Oualid, F. Kosior, A. Dauscher, C. Candolfi, G. Span, E. Mehmedovic, J. Paris, B. Lenoir, *Energy Environ. Sci.* **2020**, *13*, 3579.

[35] Q. Xu, S. Qu, C. Ming, P. Qiu, Q. Yao, C. Zhu, T.-R. Wei, J. He, X. Shi and L. Chen, *Energy Environ. Sci.*, 2020, **13**, 511–518.

[36] Y. Qi and M. C. McAlpine, *Energy Environ. Sci.*, 2010, **3**, 1275–1285.

[37] M. He, J. Ge, Z. Lin, X. Feng, X. Wang, H. Lu, Y. Yang, F. Qiu, *Energy Environ. Sci*., **2012**, *5*, 8351.

[38] C. Wan, X. Gu, F. Dang, T. Itoh, Y. Wang, H. Sasaki, M. Kondo, K. Koga, K. Yabuki, G. J. Snyder, R. Yang, K. Koumoto, *Nat. Mater.* **2015**, *14*, 622.

[39] Y. Lu, Y. Qiu, K. Cai, Y. Ding, M. Wang, C. Jiang, Q. Yao, C. Huang, L. Chen, J. He, *Energy Environ. Sci.* **2020**, *13*, 1240.

[40] G. Hu, H. Edwards, M. Lee, *Nat. Electron.* **2019**, *2*, 300–306.

[41] R. Dhawan, P. Madusanka, G. Hu, J. Debord, T. Tran, K. Maggio, H. Edwards, M. Lee, *Nat. Commun.* **2020**, *11*, 4362.

[42] W. Zhou, Q. Fan, Q. Zhang, L. Cai, K. Li, X. Gu, F. Yang, N. Zhang, Y. Wang, H. Liu, W. Zhou, S. Xie, *Nat. Commun.* **2017**, *8*, 1.

[43] M. S. El-Genk, H. H. Saber, T. Caillat, J. Sakamoto, *Energy Convers. Manag.* **2006**, *47*, 174.

[44] H. H. Saber, M. S. El-Genk, T. Caillat, *Energy Convers. Manag.* **2007**, *48*, 555.

[45] D. Zhao, C. Tian, S. Tang, Y. Liu, L. Jiang, L. Chen, *Mater. Sci. Semicond. Process.* **2010**, *13*, 221.

[46] S. M. Choi, K.-H. Kim, S.-M. Jeong, H.-S. Choi, Y. S. Lim, W.-S. Seo, I.-H. Kim, *J. Electron. Mater.* **2012**, *41*, 1004.

[47] J. Q. Guo, H. Y. Geng, T. Ochi, S. Suzuki, M. Kikuchi, Y. Yamaguchi, S. Ito, *J. Electron. Mater.* **2012**, *41*, 1036.

[48] J. Garcia-Canadas, A. V. Powell, A. Kaltzoglou, P. Vaqueiro, G. Min, *J. Electron. Mater.* **2013**, *42*, 1369.

[49] T. Ochi, G. Nie, S. Suzuki, M. Kikuchi, S. Ito, J. Q. Guo, *J. Electron. Mater.* **2014**, *43*, 2344.

[50] J. R. Salvador, J. Cho, Z. Ye, A. Thompson, J. Sharp, J. Konig, R. Maloney, T. Thompson, J. Sakamoto, H. Wang, A. A. Wereszczak, *Phys. Chem. Chem. Phys.* **2014**, *16*, 12510.

[51] E. Alleno, N. Lamquembe, R. Cardoso-Gil, M. Ikeda, F. Widder, O. Rouleau, C. Godart, Yu. Grin, S. Paschen, *Phys. Status Solidi A* **2014**, *211*, 1293.

[52] G. Nie, S. Suzuki, T. Tomida, A. Sumiyoshi, T. Ochi, K. Mukaiyama, M. Kikuchi, J. Q. Guo, A. Yamamoto, H. Obara, *J. Electron. Mater.* **2017**, *46*, 2640.

[53] Q. Zhang, Z. Zhou, M. Dylla, M. T. Agne, Y. Pei, L. Wang, Y. Tang, J. Liao, J. Li, S. Bai, W. Jiang, L. Chen, G. J. Snyder, *Nano Energy* **2017**, *41*, 501.

[54] P. Zong, R. Hanus, M. Dylla, Y. Tang, J. Liao, Q. Zhang, G. J. Snyder, L. Chen, *Energy Environ. Sci.* **2017**, *10*, 183.

[55] J. Prado-Gonjal, M. Phillips, P. Vaqueiro, G. Min, A. V. Powell, *ACS Appl. Energy Mater.* **2018**, *1*, 6609.

[56] S. Katsuyama, W. Yamakawa, Y. Matsumara, R. Funahashi, *J. Electron. Mater.* **2019**, *48*, 5257.

[57] G. Rogl, L. Zhang, P. Rogl, A. Grytsiv, M. Falmbigl, D. Rajs, M. Kriegisch, H. Müller, E. Bauer, J. Koppensteiner, W. Schranz, M. Zehetbauer, Z. Henkie, M. B. Maple, *J. Appl. Phys.* **2010**, *107*, 043507.

[58] A. Reuss, *Z. Angew. Math. Mech.* **1929**, *9*, 49.

[59] P. Canale, C. Servant, *Z. Metallkd.* **2002**, *93*, 273.

[60] D. Qin, H. Wu, S. Cai, J. Zhu, B. Cui, L. Yin, H. Qin, W. Shi, Y. Zhang, Q. Zhang, W. Liu, J. Cao, S. J. Pennycook, W. Cai, J. Sui, *Adv. Energy Mater.* **2019**, *9*, 1902435.

[61] Y. Tang, Z. M. Gibbs, L. A. Agapito, G. Li, H.-S. Kim, M. B. Nardelli, S. Curtarolo, G. J. Snyder, *Nat. Mater.* **2015**, *14*, 1223.

[62] M. Puyet, B. Lenoir, A. Dauscher, C. Candolfi, J. Hejtmanek, *Appl. Phys. Lett.* **2012**, *101*, 222105.

[63] J. Leszczynski, V. Da Ros, B. Lenoir, A. Dauscher, C. Candolfi, P. Masschelein, J. Hejtmanek, K. Kutorasinski, J. Tobola, R. I. Smith, C. Stiewe, E. Müller, *J. Phys. D: Appl. Phys.* **2013**, *46*, 495106.

[64] M. Benyahia, V. Ohorodniichuk, E. Leroy, A. Dauscher, B. Lenoir, E. Alleno, J. Alloys Compnds **2018**, *735*, 1096.

[65] Rodriguez-Carvajal, J. *Physica B* **1993**, *192*, 55.

[66] W. Voigt, *Annalen der Physik* **1889**, *274*, 573.

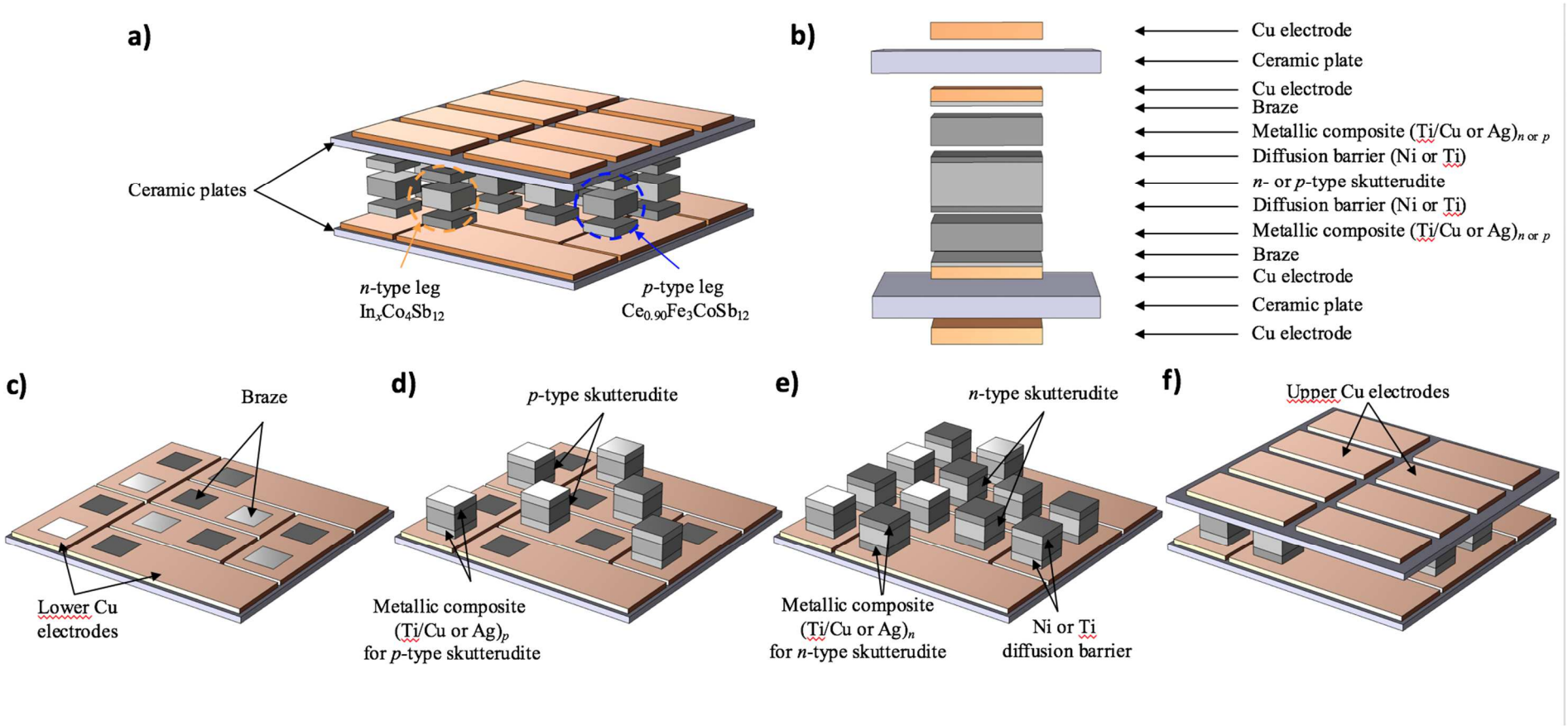

Fig. 1. Fabrication process of the skutterudite-based thermoelectric modules. **a)** Expanded view of an illustrative six-couple TEG made of *n*-type and *p*-type skutterudites connected electrically in series and thermally in parallel. **b)** Non-conventional design of the thermoelectric legs composed of the skutterudites sandwiched by Ni or Ti layers acting as diffusion barriers and Ti/Cu or Ti/Ag metallic composites that accommodate differences in the

lattice thermal expansion between the skutterudites and the Cu metallic contacts and favor the brazing step. **c to f**) Steps of the assembly for an illustrative six-couple TEG. The InCuSil braze is applied on the lower Cu-Ni paths (**c**), deposited on an Al_2O_3 ceramic plate, to electrically connect the *p*- (**d**) and *n*-type (**e**) thermoelectric legs fabricated by spark plasma sintering. The second, upper ceramic plate is then brazed on the assembly (**f**).

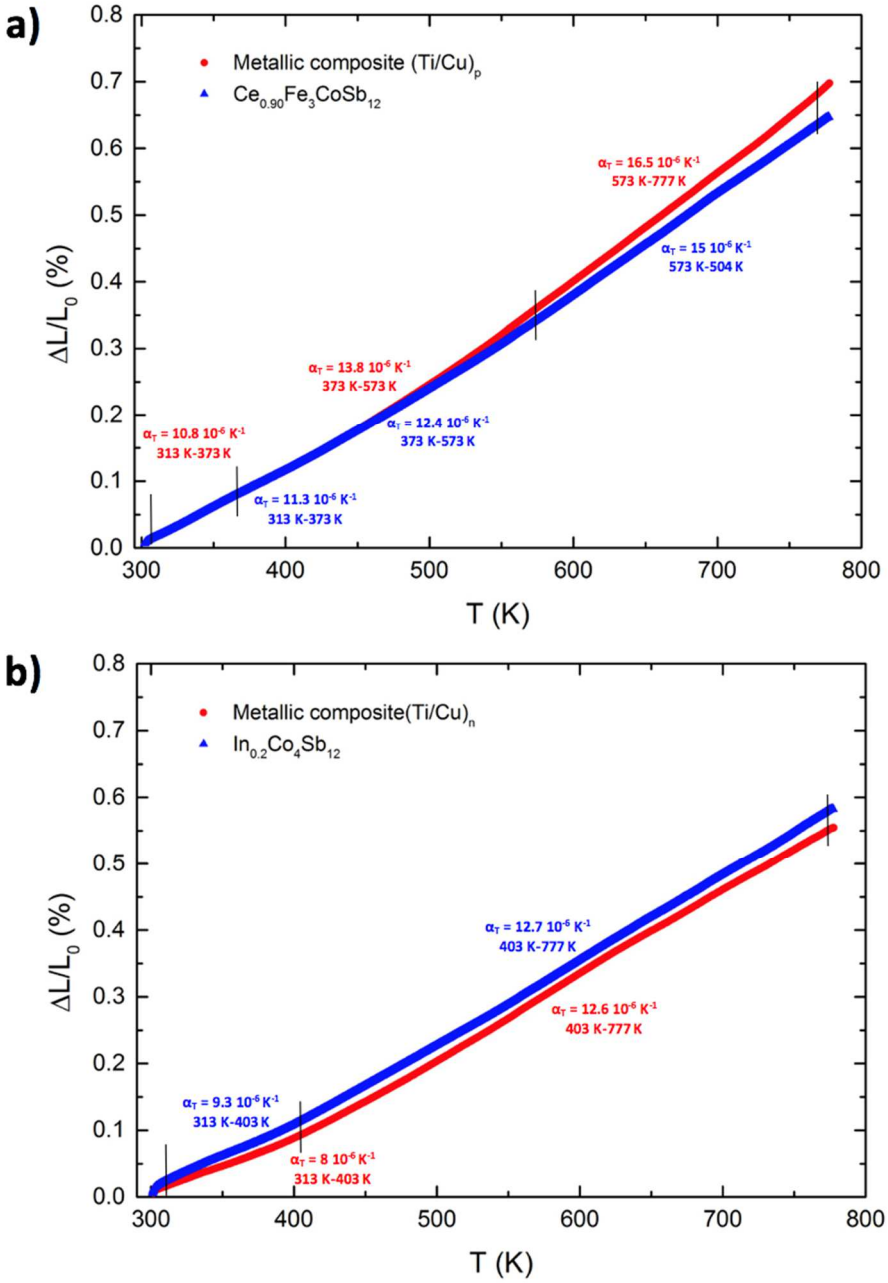

Fig. 2. Thermal expansion $\Delta L/L_0$ of the (**a**) *n*-type and (**b**) *p*-type skutterudites as a function of temperature. The temperature dependence of the thermal expansion of the $(Ti/Cu)_n$ and $(Ti/Cu)_p$ metallic composites are also shown for comparison. For each material, the thermal expansion coefficients $\alpha_T = \frac{1}{L_0}\left(\frac{\partial \Delta L}{\partial T}\right)$ is indicated in the different temperature ranges highlighted by the vertical black lines.

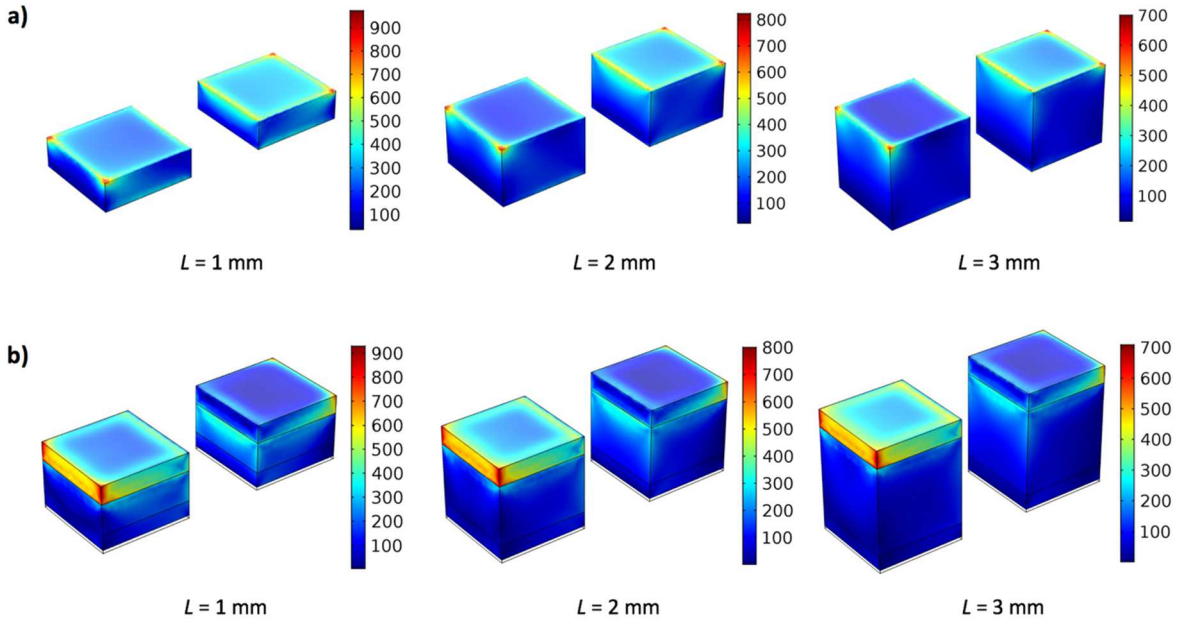

Fig. 3. Distribution of the equivalent von Mises stresses calculated by three-dimensional finite element analyses on a single couple of *p*- (left parallelepipeds) and *n*-type (right parallelepipeds) skutterudites for an illustrative $\Delta T = 500$ K and for $L = 1$, 2 and 3 mm. These calculations were performed **a)** without and **b)** with $(Ti/Cu)_{n,p}$ metallic composites.

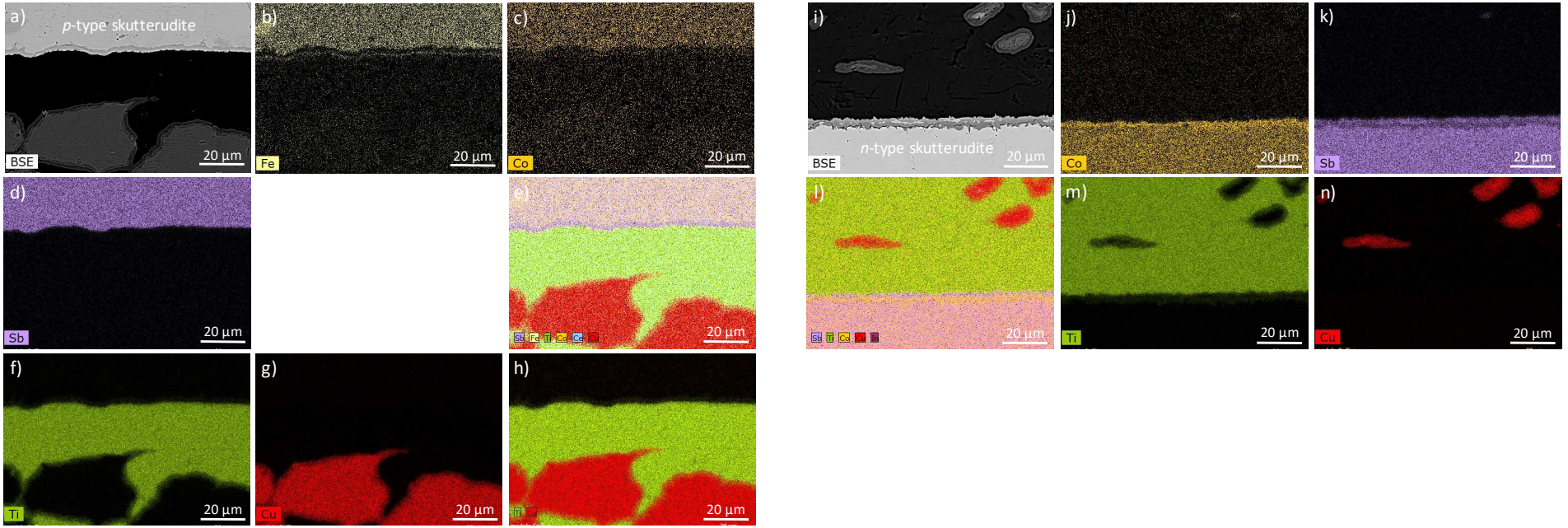

Fig. 4. SEM images and elemental X-ray maps of the thermoelectric legs composed of the *p*-type (panels **a** to **h**) and *n*-type (panels **i** to **n**) skutterudites sandwiched by the (Ti/Cu) metallic composites and the Ti diffusion barrier. *p*-type and *n*-type skutterudites are at the top and bottom of the images respectively. The panels **e**, **h** and **l** correspond to overlaid images of several X-ray maps as indicated in the legend (left bottom). These analyses evidence the formation of several intermetallic compounds forming an interfacial reaction layer that prevents the migration of the elements. Note that the X-ray map of Ce is not shown due to the emission line of Ce being very close to that of Ti.

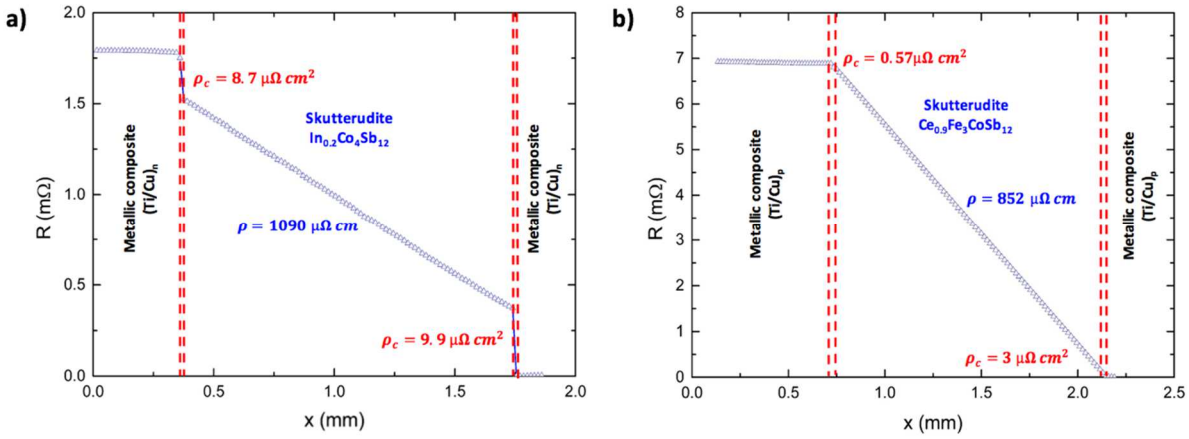

Fig. 5. Electrical contact resistance of the spark-plasma-sintered skutterudite legs. The electrical contact resistance ρ_c of the (**a**) *n*-type and (**b**) *p*-type skutterudite legs highlights the excellent control of the interfaces achieved with no obvious significant drop at the interfaces (see Figure S12 in SI for sketches of imperfect contacts), represented as vertical dotted lines, on going from the $(Ti/Cu)_{n,p}$ metallic composites to the skutterudite through the Ti layer. The slopes of the three linear lines correspond to the electrical resistivity of the materials. The values inferred from these measurements are in very good agreement with those measured on each material separately.

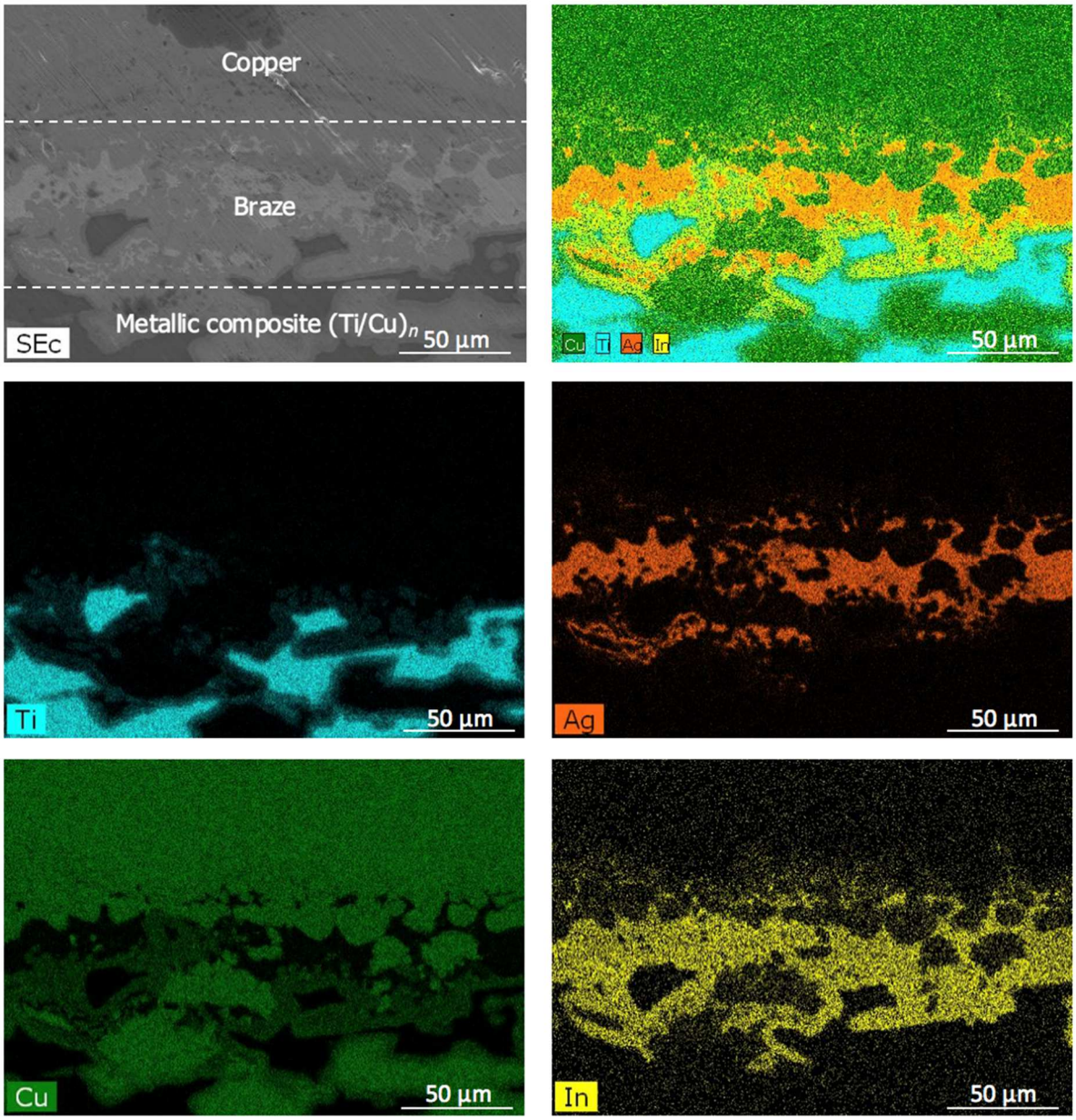

Fig. 6. SEM images and corresponding elemental X-ray maps of the interfaces between the metallic composites of the legs and the Cu-Ni interconnections after completion of the brazing process using InCuSil.

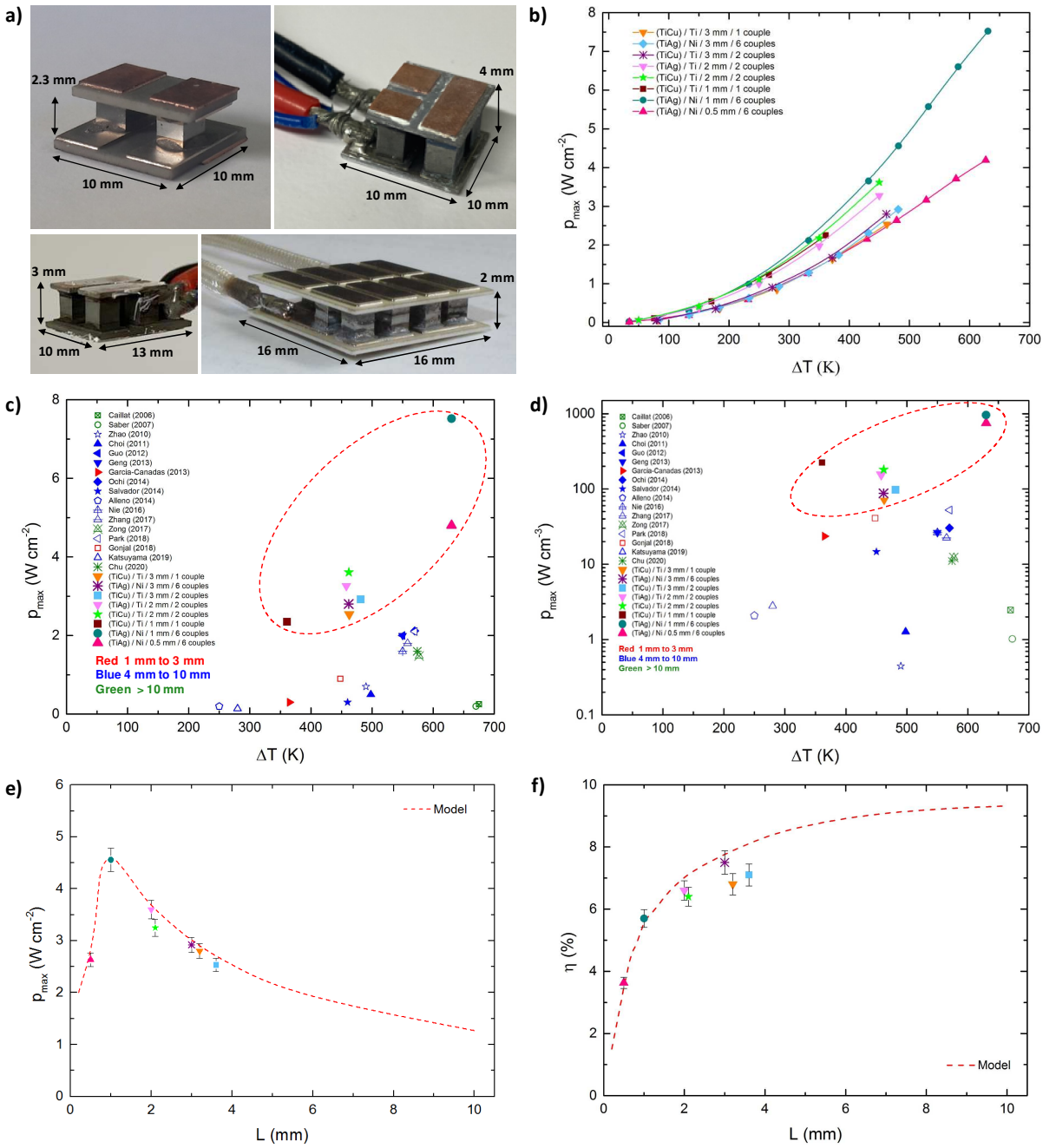

Fig. 7. a) Photographs illustrating three TEGs integrating skutterudites, representative of the various TEGs fabricated and tested in this study: (upper left) a single-couple TEG with $(Ti/Cu)_{n,p}$ metallic composite and Ti diffusion barrier with skutterudite layers of 1 mm, (upper right) a two-couple TEG with $(Ti/Cu)_{n,p}$ metallic composite and Ti diffusion barrier with skutterudite layers of 3 mm, (bottom left) a two-couple TEG with $(Ti/Cu)_{n,p}$ metallic composite and Ti diffusion barrier with skutterudite layers of 2 mm, (bottom right) and a six-couple TEG $(Ti/Ag)_{n,p}$ metallic composite and Ni diffusion barrier with skutterudite layers of 1 mm. b)

Maximum power density p_{max} of various TEGs measured experimentally as a function of the applied temperature difference ΔT. For two of them, the measurements were collected up to $\Delta T = 630$ K. **c)** Comparison of the maximum output power density p_{max} expressed in W cm^{-2} achieved in the present study with the literature data (Refs. 14, 15 and 43-56) as a function of the temperature difference ΔT applied. Red, blue and green symbols correspond to length of the legs varying between 1 and 3 mm, 4 mm and 10 mm and above 10 mm, respectively. The results obtained in the present study are encircled in red. **d)** Comparison of the maximum output power density p_{max} as a function of the applied temperature difference ΔT per unit volume of skutterudites, allowing for a straightforward comparison between devices integrating skutterudite legs of various lengths. Note the logarithmic scale of the *y* axis. The results obtained in the present study are encircled in red. **e)** Prediction of the variations in the maximum output power density p_{max} as a function of the length of the skutterudites *L* determined by finite-element analyses. The theoretical red dotted curve has been calculated using hot side $T_h = 483$ K and cold side $T_c = 33$ K temperatures, electrical contact resistances $\rho_{c,p} = 12.9$ μΩ cm^2 and $\rho_{c,n} = 15.2$ μΩ cm^2 of the *p* and *n*-type legs, respectively, and an interface thermal resistance $R_{th} = 4\times10^{-4}$ K m^{-2} W^{-1} between the module and the reservoir. The experimental points measured on the various TEGs have been added. p_{max} significantly increases upon shortening the length of the skutterudites. The maximum value, achieved around 1 mm, drops if the length is further reduced due to the detrimental influence of the thermal resistances of the metallic composite layers.

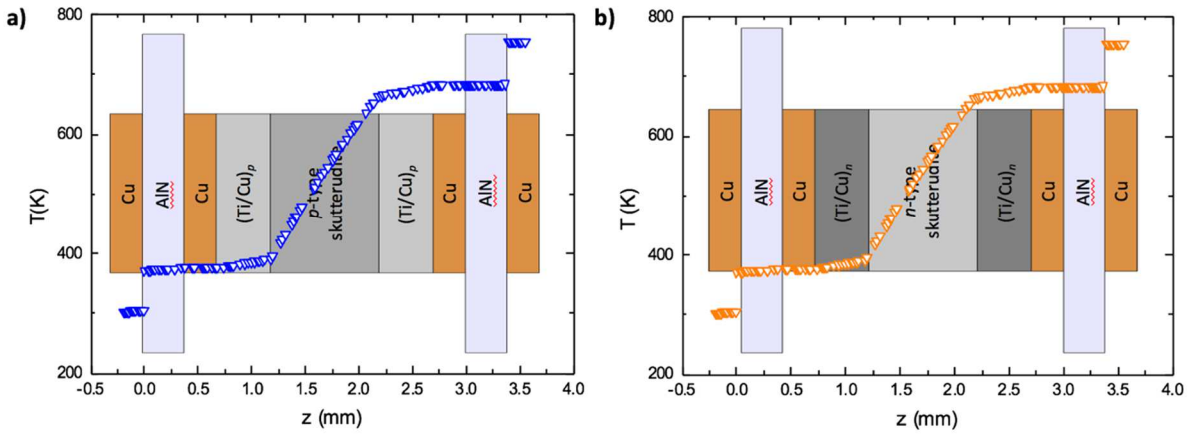

Fig. 8. Evolution of the temperature on the *p*- and *n*-type skutterudite legs calculated by finite-element analyses. The temperature profiles on the (**a**) *p*- and (**b**) *n*-type legs induced by the temperature difference ΔT of 450 K imposed between the hot and cold reservoirs. For sake of clarity, the structures of the legs are overlaid. Due to differences in thermal conductances of the different materials (mainly the ceramic plates), the skutterudite layers are not subjected to the imposed ΔT but to a fraction of it, which amounts to around 64 and 61% for the *p* and *n*-type legs, respectively. Except for the temperature drop due to the external contacts between the module and the hot and cold reservoirs (28 and 31% of ΔT for the *p* and *n*-type legs, respectively), the main drops in temperature occur across the $(Ti/Cu)_{n,p}$ metallic composites (around 8% of ΔT for both legs). Lowering these temperature drops would increase the temperature difference undergone by the skutterudite layers and hence, the maximum output power p_{max} delivered by the thermoelectric generator.

An innovative approach for designing high-power-density thermoelectric generator is presented. Inserting metallic composite layers in the thermoelectric legs enables a drastic decrease in their length, yielding record-breaking power densities for skutterudite-based generators. This novel design will allow for a strong reduction of the volume of thermoelectric materials integrated while concomitantly achieving higher power density.

Keyword: Thermoelectrics

*S. El Oualid, I. Kogut, M. Benyahia, E. Geczi, U. Kruck, F. Kosior, P. Masschelein, C. Candolfi, A. Dauscher, J. D. Koenig, A. Jacquot, T. Caillat, E. Alleno, B. Lenoir**

High Power Density Thermoelectric Generators with Skutterudites

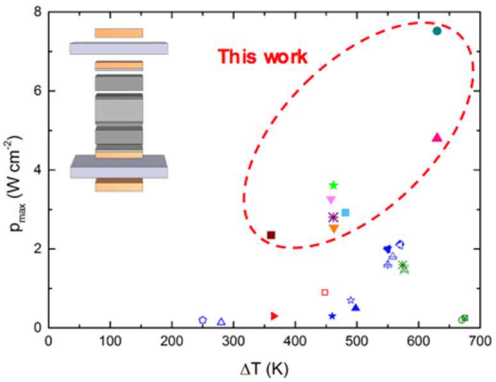

Supporting Information

High Power Density Thermoelectric Generators with Skutterudites

*Soufiane El Oualid, Iurii Kogut, Mohamed Benyahia, Eugen Geczi, Uwe Kruck, Francis Kosior, Philippe Masschelein, Christophe Candolfi, Anne Dauscher, Jan Dieter Koenig, Alexandre Jacquot, Thierry Caillat, Eric Alleno, Bertrand Lenoir**

Materials	Poisson ratio	CTE @ 300K	Young modulus (GPa)	Yield stress (MPa)	Tensile Strength (MPa)	Hardening rate (GPa)
$Ce_{0.85}Fe_3CoSb_{12}$	0.23	11.3	144	-	506	-
AlN	0.23 (Ref. 1)	5 (Ref. 1)	310 (Ref. 1)	-	200 (Ref. 2)	-
Al_2O_3	0.26 (Ref. 1)	7.5 (Ref. 1)	350 (Ref. 1)	-	416 (Ref. 2)	-
$In_xCo_4Sb_{12}$	0.2	9.3	157	-	637	-
$(Ti/Cu)_n$	0.34	8	124	229	-	1.14
$(Ti/Cu)_p$	0.33	10.8	119	179	-	0.97
$(Ti/Ag)_n$	0.32	10	111	233	-	0.95
$(Ti/Ag)_p$	0.30	11	82	141	-	0.54
Cu	0.35 (Ref. 3)	16.5 (Ref. 3)	128 (Ref. 3)	70	-	0.8

Table S1. Mechanical and thermal properties of materials at 300 K used in the mechanical modelling. (Young modulus for all, Poisson ratio for all, Yield stress for metals (Cu and metallic composites), Tensile strength for AlN and the skutterudites and the thermal expansion coefficient CTE).

References for Table S1

(1) Radosavljevic, G.; Smetana. W. Printed heater elements, Woodhead Publishing Series in Electronic and Optical Materials, Printed Films, p. 429–468, 2012.

(2) Hirao, K.; Zhou, Y.; Miyazaki, H. Substrate, Woodhead Publishing Series in Electronic and Optical Materials, Wide Bandgap Power Semiconductor Packaging, p. 81–94, 2018.

(3) Rajaguru, P.; Lu, H.; Bailey, C. Sintered silver finite element modelling and reliability based design optimization in power electronic module, Microelectronics Reliability. Vol. 55, p. 919–930, 2015.

2). Equations of η taking into account contact resistances and evolution of η as a function of the length L of the skutterudites.

As mentioned in the introduction of the main text, the maximum output power P_{max} of a single-couple TEG is obtained when the impedance matching condition is achieved and is expressed as

$$P_{max} = \frac{S(\alpha_p - \alpha_n)^2 \Delta T^2}{4L(\rho_n + \rho_p)} \tag{6}$$

Under realistic conditions, both finite thermal and electrical resistances at the interfaces should be taken into account, yielding the following expression of P_{max}

$$P_{max}^c = \frac{S(\alpha_p - \alpha_n)^2 \Delta T^2}{4(\rho_n + \rho_p)(n + L)(1 + 2rl_c/L)^2} \tag{7}$$

where $n = 4\rho_c/(\rho_n + \rho_p)$ with ρ_c the electrical contact resistance, $r = (\kappa_n + \kappa_p)/2\kappa_c$ with κ_c the effective thermal conductivity of the contact layer and l_c is the thickness of the contact layer. The effect of the contact resistances can be obtained by the ratio of these two quantities

$$P_c = \frac{P_{max}^c}{P_{max}} = \frac{1}{\left(1 + \frac{n}{L}\right)\left(1 + 2r\frac{l_c}{L}\right)^2} \tag{8}$$

When P_{max}^c is achieved, the corresponding conversion efficiency η_c is given by the following expression

$$\eta_c = \frac{\left(\frac{T_H - T_C}{T_H}\right)}{\left(1 + 2r\frac{l_c}{L}\right)^2 \left(2 - \frac{1}{2}\left[\frac{T_H - T_C}{T_H}\right] + \left(\frac{4}{Z_{np}T_H}\right)\left(\frac{1 + \frac{n}{L}}{1 + 2r\frac{l_c}{L}}\right)\right)} \quad (9)$$

where T_H and T_C are the hot-side and cold-side temperatures, respectively, and Z_{np} is the thermoelectric figure of merit of the *n-p* couple defined as

$$Z_{np} = \frac{(\alpha_p - \alpha_n)^2}{(\kappa_n + \kappa_p)(\rho_n + \rho_p)} \quad (10)$$

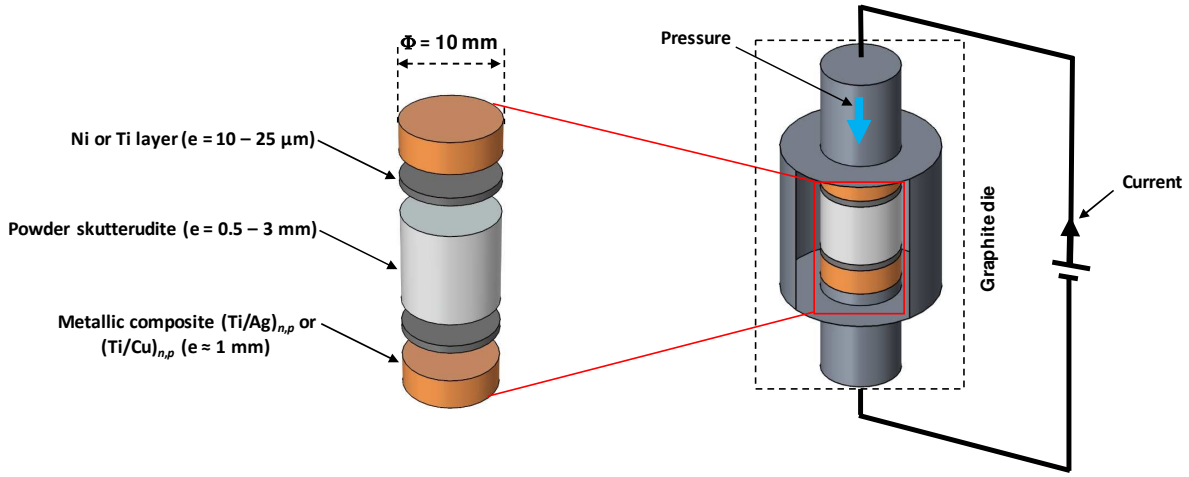

Figure S1. Sketch of the spark plasma sintering process. Dense cylindrical pellets of *p*- or *n*-type skutterudites of 10 mm in diameter, sandwiched by Ni or Ti diffusion barriers and $(Ti/Ag)_{n,p}$ or $(Ti/Cu)_{n,p}$ metallic composites, are placed in a graphite die. The assembly is subjected to a pressure-temperature cycle optimized to achieve good electrical contacts with flat interfaces between the different layers.

3). Characterization of a six-couple skutterudite-based TEG with $(Ti/Ag)_{n,p}$ metallic composites and Ni as a diffusion barrier.

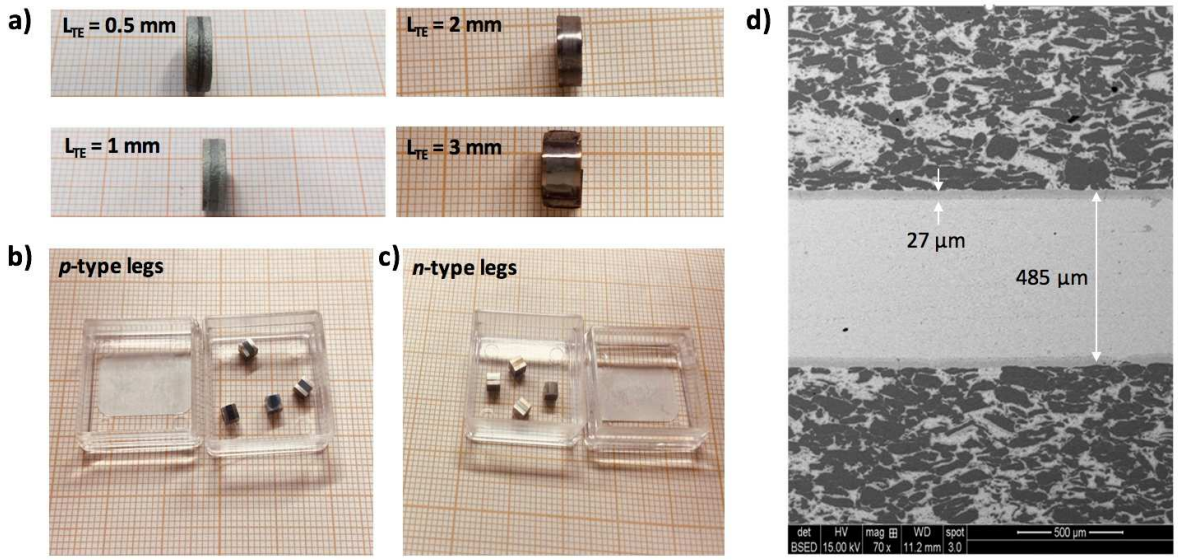

Figure S2. Photographs and scanning electron microscopy image of the fabricated *p*- and *n*-type skutterudite legs. The cylindrical pellets (**a**), consisting in the skutterudites sandwiched by the Ni layer and $(Ti/Ag)_{n,p}$ metallic composites, were diced into cubes with section areas of 2×2 mm^2 (**b**, **c**). An example of the flat interfaces obtained for a skutterudite height of 485 µm is given by scanning electron microscopy (**d**). The Ni diffusion barriers are on either side of the skutterudite with a height of ~27 µm. Beyond the Ni barrier is the metallic composite made of a mixture of Ti/Ag.

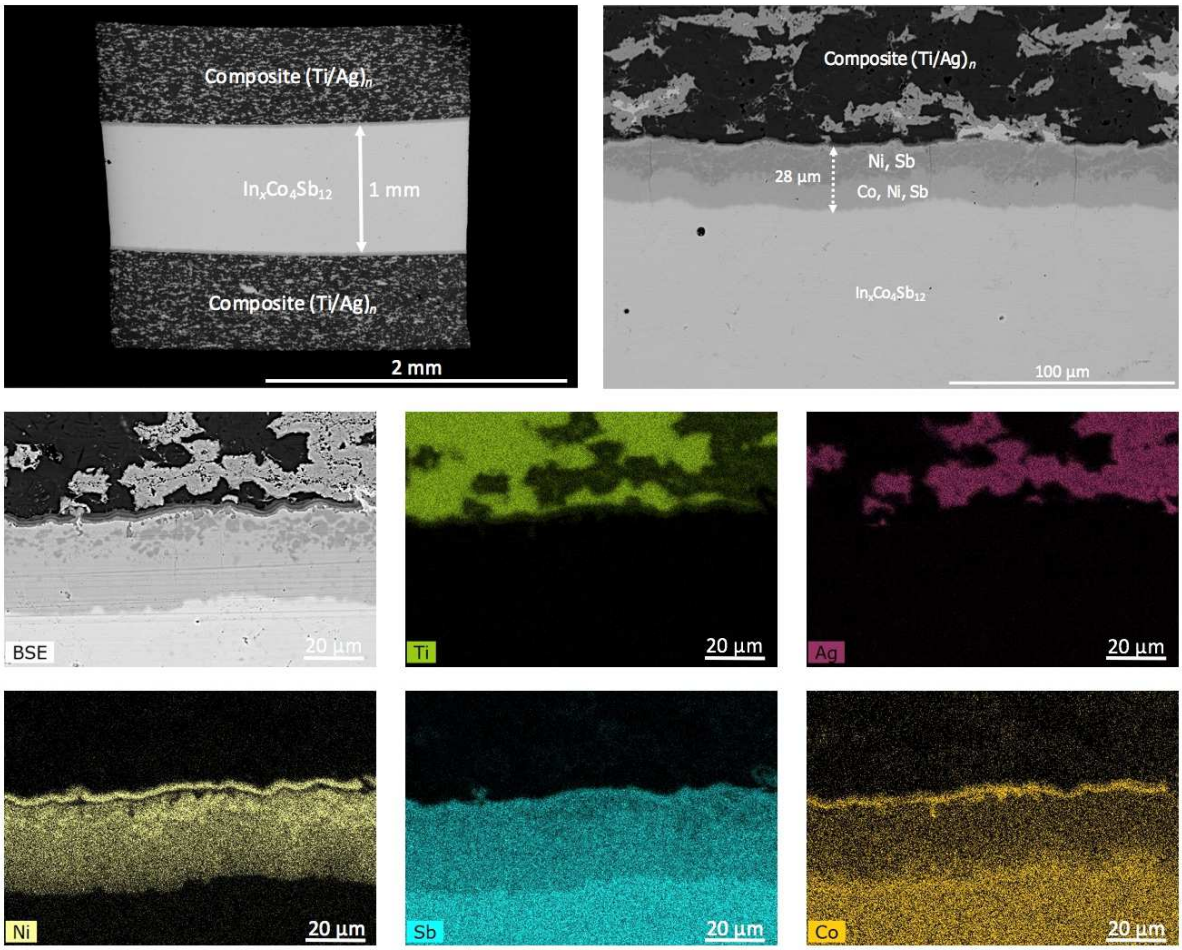

Figure S3. (Upper row) Scanning electron microscopy images of the *n*-type leg composed of *n*-type skutterudite sandwiched by $(Ti/Ag)_n$ metallic composites and Ni as the diffusion barrier. (Middle and lower rows) SEM image collected in the backscattered electron mode (BSE) together with the corresponding elemental X-ray maps.

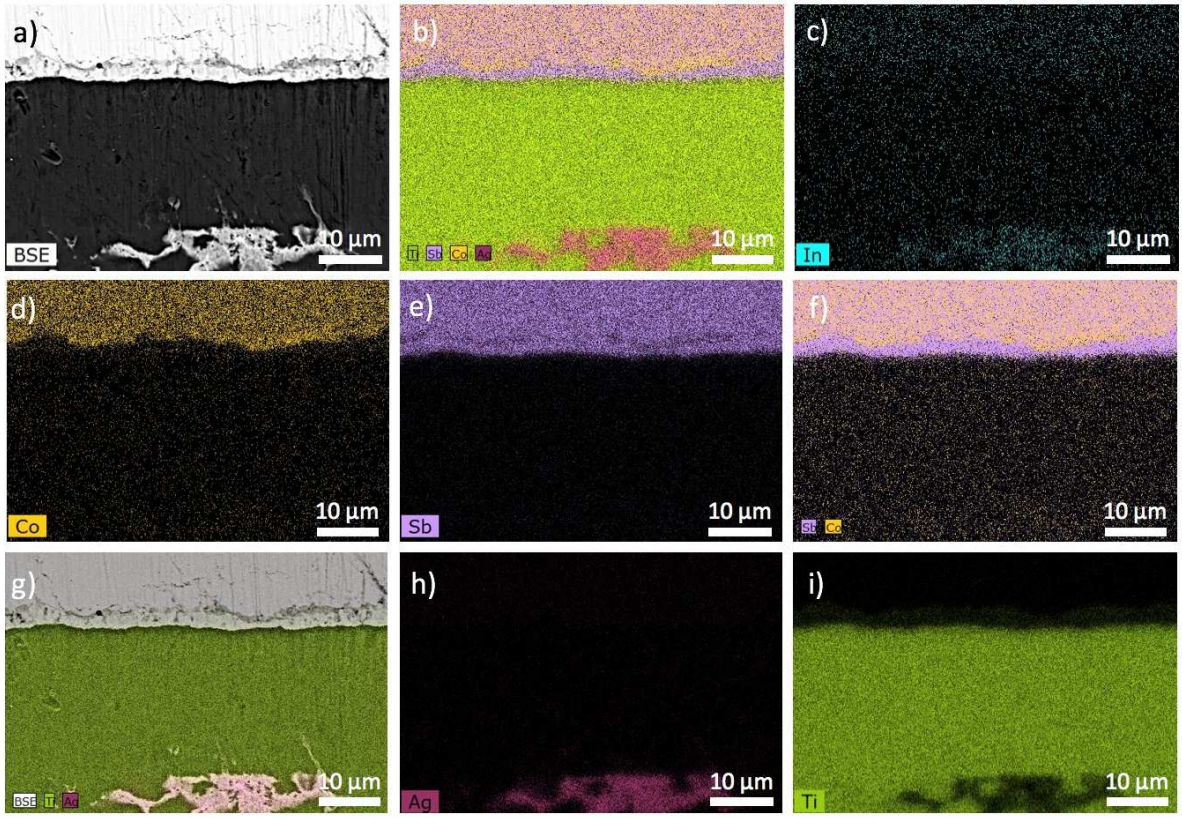

Figure S4. Scanning electron microscopy images collected in the backscattered electron mode (a) of the interface between the *n*-type skutterudite and the $(Ag/Ti)_n$ metallic composite. The corresponding elemental X-ray maps are shown in panels c) to i) with overlaid images shown in panel b) and g). Note that the emission line of In is close to that of Ag, explaining the seeming presence of In in the Ag layer.

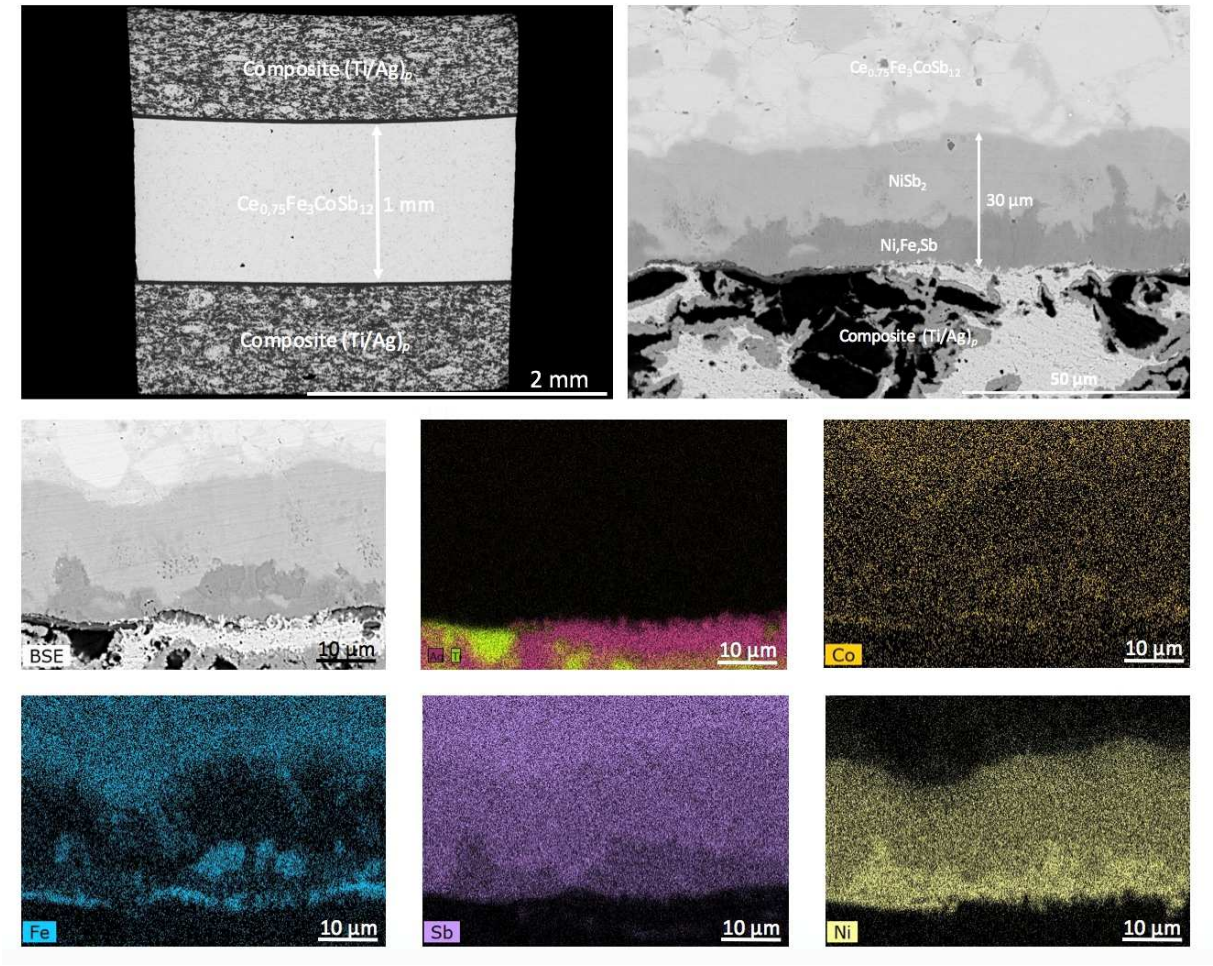

Figure S5. (Upper row) Scanning electron microscopy images of the *p*-type leg composed of *p*-type skutterudite sandwiched by $(Ti/Ag)_p$ metallic composites and Ni as the diffusion barrier. (Middle and lower rows) SEM image collected in the backscattered electron mode (BSE) together with the corresponding elemental X-ray maps.

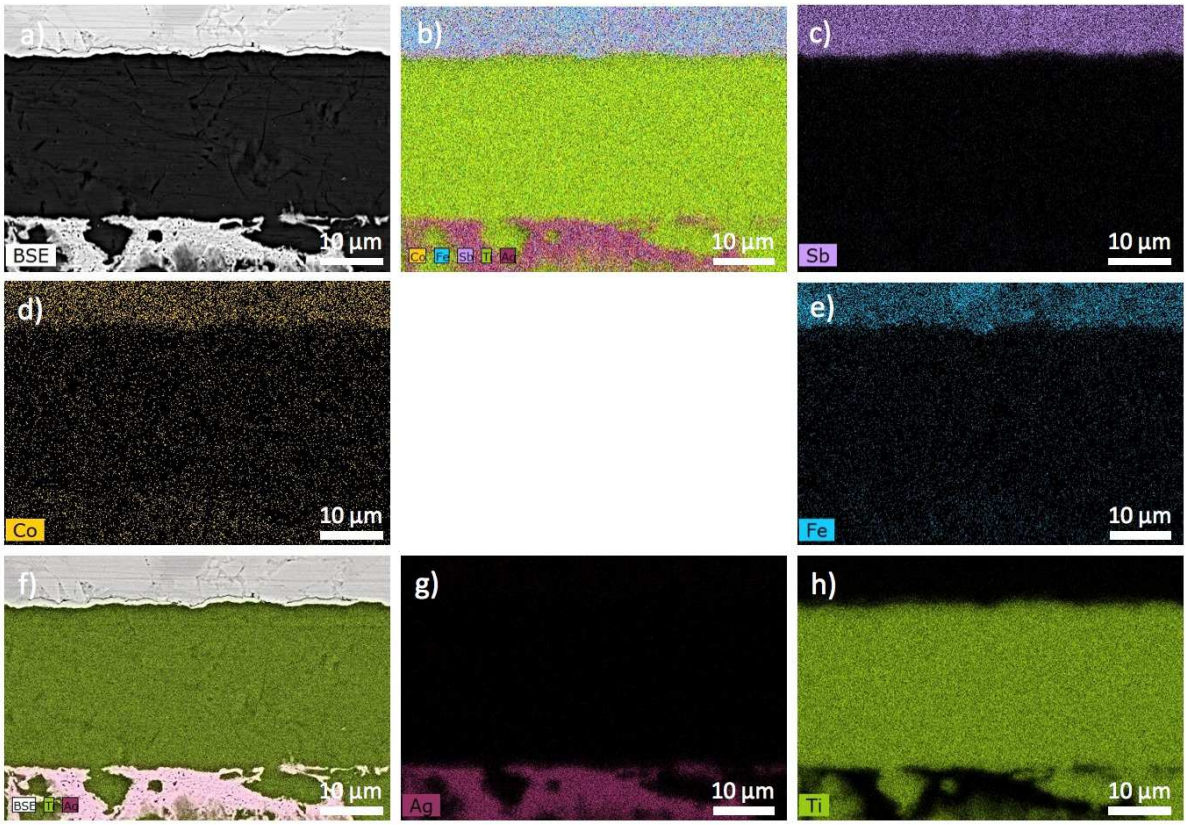

Figure S6. Scanning electron microscopy images collected in the backscattered electron mode (a) of the interface between the *n*-type skutterudite and the $(Ag/Ti)_p$ metallic composite. The corresponding elemental X-ray maps are shown in panels c) to h) with overlaid images shown in panel b) and f). The X-ray map of Ce is not shown due to the emission line of Ce, which is very close to that of Ti.

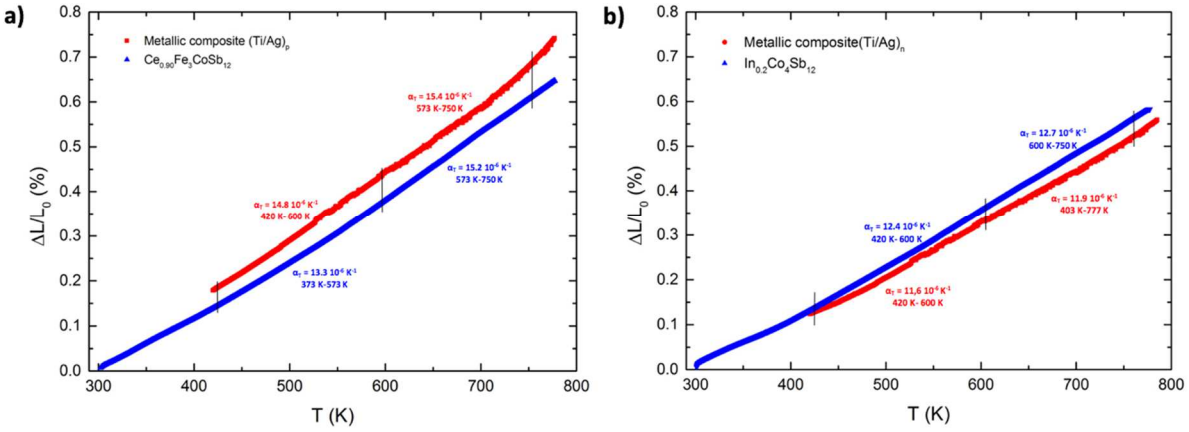

Figure S7. Thermal expansion $\Delta L/L_0$ of the (a) *p*-type and (b) *n*-type skutterudites as a function of temperature. The temperature dependence of the thermal expansion of the $(Ti/Ag)_n$ and $(Ti/Ag)_p$ metallic composites are also shown for comparison. For each material, the thermal expansion coefficient $\alpha_T = \frac{1}{L_0}\left(\frac{\partial \Delta L}{\partial T}\right)$ are indicated in the different temperature ranges highlighted by the vertical black lines.

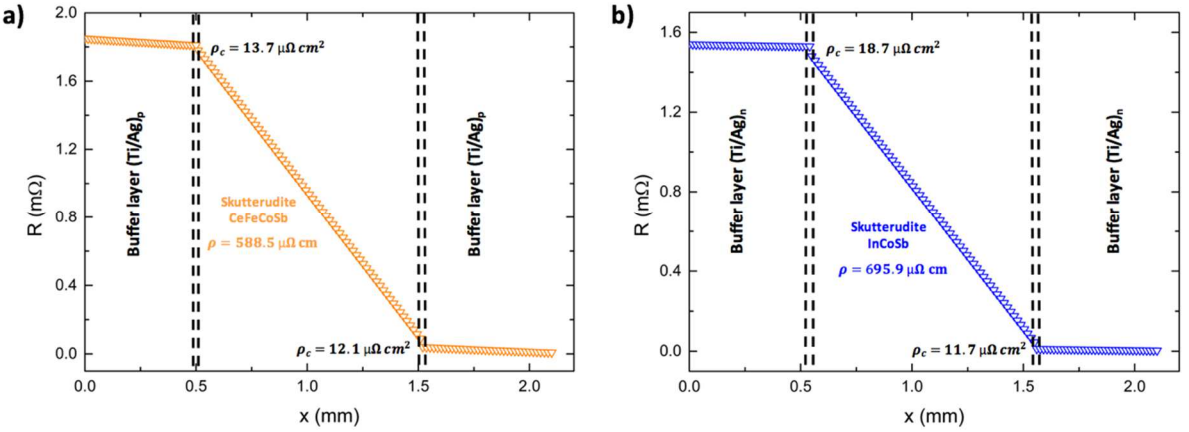

Figure S8. Electrical contact resistance of the spark-plasma-sintered skutterudite legs for the modules composed of (Ag/Ti)*n,p* metallic composites. The electrical contact resistance ρ_c of the (**a**) *p*-type and (**b**) *n*-type skutterudite legs highlights the excellent control of the interfaces achieved with no obvious significant drop at the interfaces (see Figure S11 in SI for sketches of imperfect contacts), represented as vertical dotted lines, on going from the $(Ag/Ti)_{n,p}$ metallic composites to the skutterudite through the Ni layer.

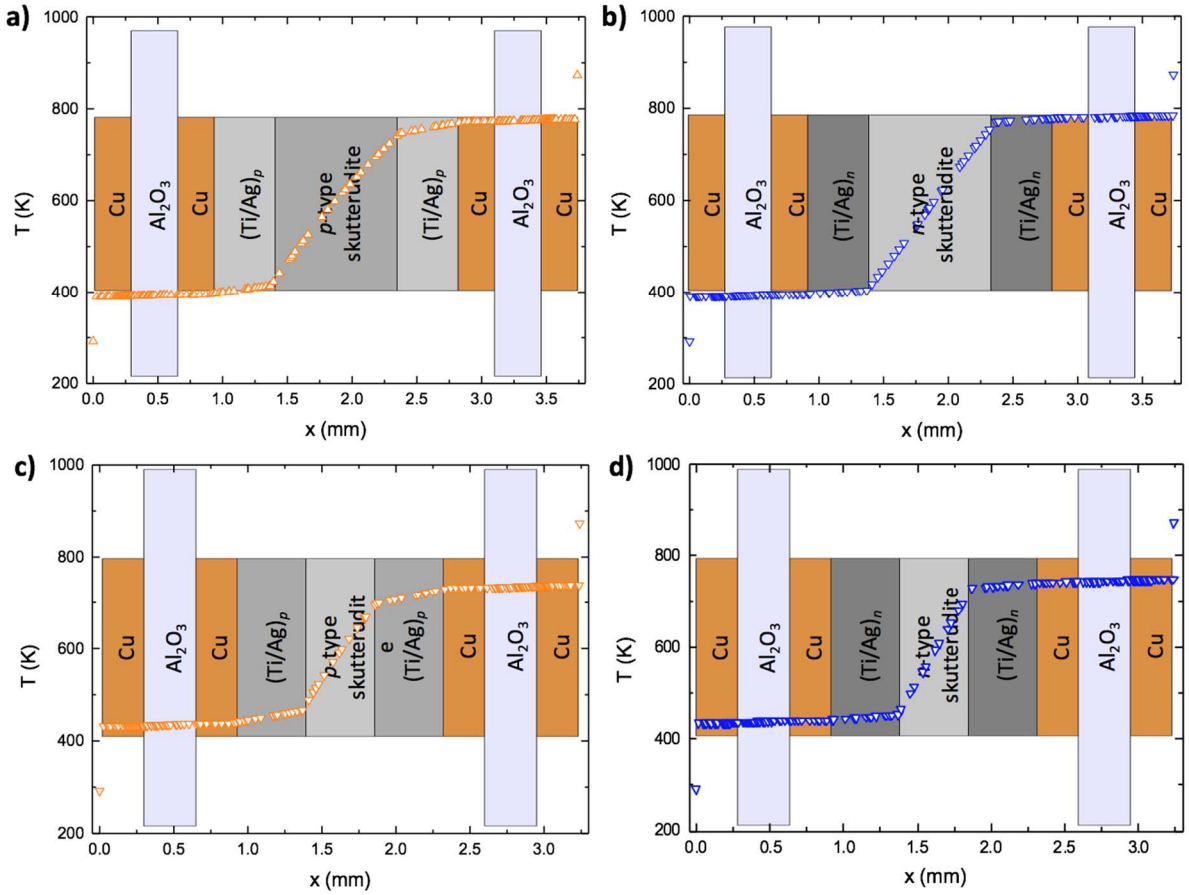

Figure S9. Evolution of the temperature on the 1-mm (panels a and b) and 0.5-mm-long (panels c and d) *p*- and *n*-type skutterudite legs of the module composed of (Ag/Ti)*n,p* metallic composites calculated by finite-element analyses.

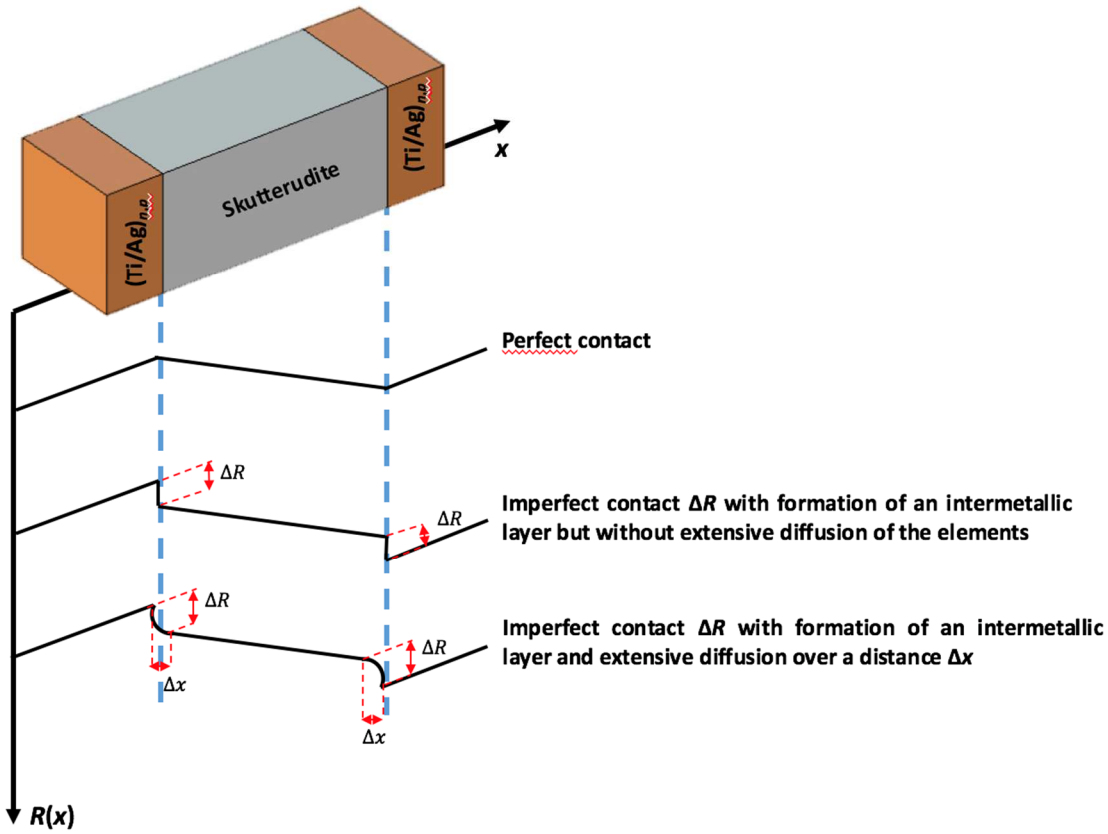

Figure S10. Sketch of the evolution of the resistance R as a function of the length x for various types of interfaces. In the case of perfect contacts between the different layers (**a**), no drop is observed at the interfaces between the skutterudite and the buffer layers. In contrast, a drop in the resistance ΔR will occur in the case of imperfect electrical contact (**b**) due to the formation of a thin layer of intermetallic compounds at the interfaces. The non-linear shape of the drop at the interface in the $R(x)$ curve occurs when extensive diffusion of the elements occurs giving rise to a larger layer of intermetallic compounds extending over a distance Δx. Thus, the overall evolution of the $R(x)$ curve can be used to determine the quality of the interfaces achieved during the SPS process.

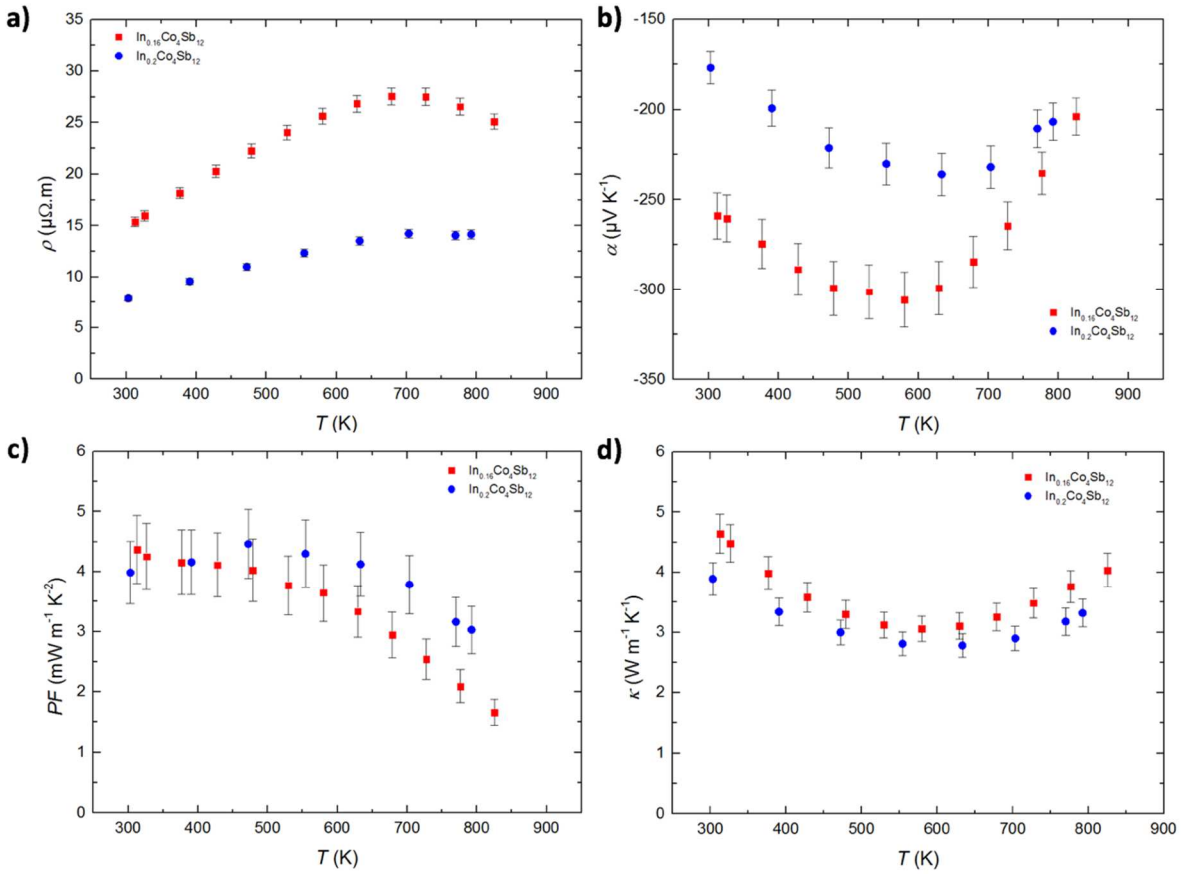

Figure S11. Temperature dependence of the thermoelectric properties of the *n*-type skutterudites. The temperature dependences of the (**a**) electrical resistivity ρ, (**b**) thermopower α, (**c**) power factor PF and (**d**) thermal conductivity κ for the *n*-type skutterudites ($In_{0.16}Co_4Sb_{12}$ and $In_{0.2}Co_4Sb_{12}$) are consistent with the literature data. In each panel, the error bars correspond to the experimental uncertainty estimated to be 3% for ρ, 5% for α, 7% for κ and 13% for PF.

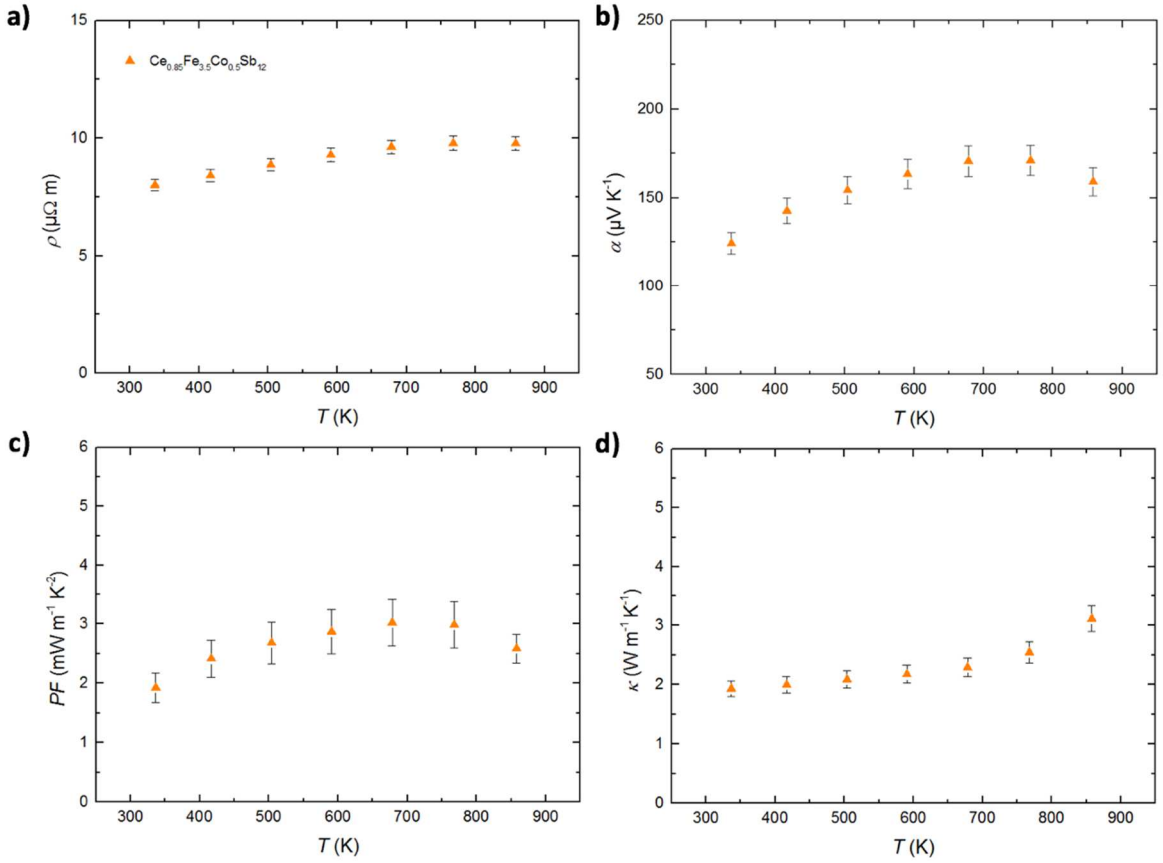

Figure S12. Temperature dependence of the thermoelectric properties of the *p*-type skutterudites. The temperature dependences of the (**a**) electrical resistivity ρ, (**b**) thermopower α, (**c**) power factor PF and (**d**) thermal conductivity κ for the *p*-type skutterudite ($Ce_{0.85}Fe_{3.5}Co_{0.5}Sb_{12}$) are consistent with the literature data. In each panel, the error bars correspond to the experimental uncertainty estimated to be 3% for ρ, 5% for α, 7% for κ and 13% for PF.

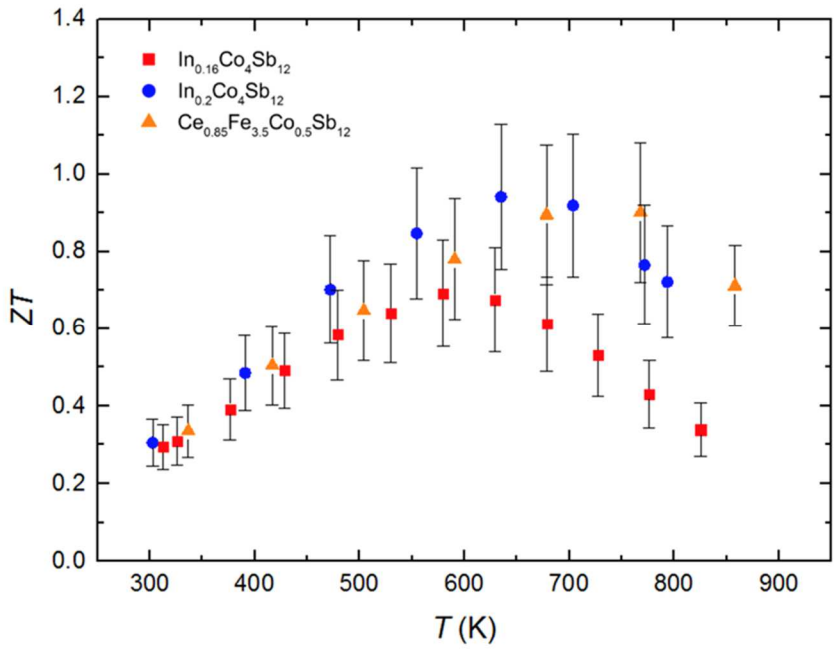

Figure S13. Temperature dependence of the dimensionless thermoelectric figure of merit *ZT* of the *n*-type and *p*-type skutterudites. The temperature dependences of the *ZT* values for the *n*-type skutterudites ($In_{0.16}Co_4Sb_{12}$ and $In_{0.2}Co_4Sb_{12}$) and for the *p*-type skutterudite ($Ce_{0.85}Fe_{3.5}Co_{0.5}Sb_{12}$) are consistent with the literature data. The error bars correspond to the experimental uncertainty estimated to be 20%.

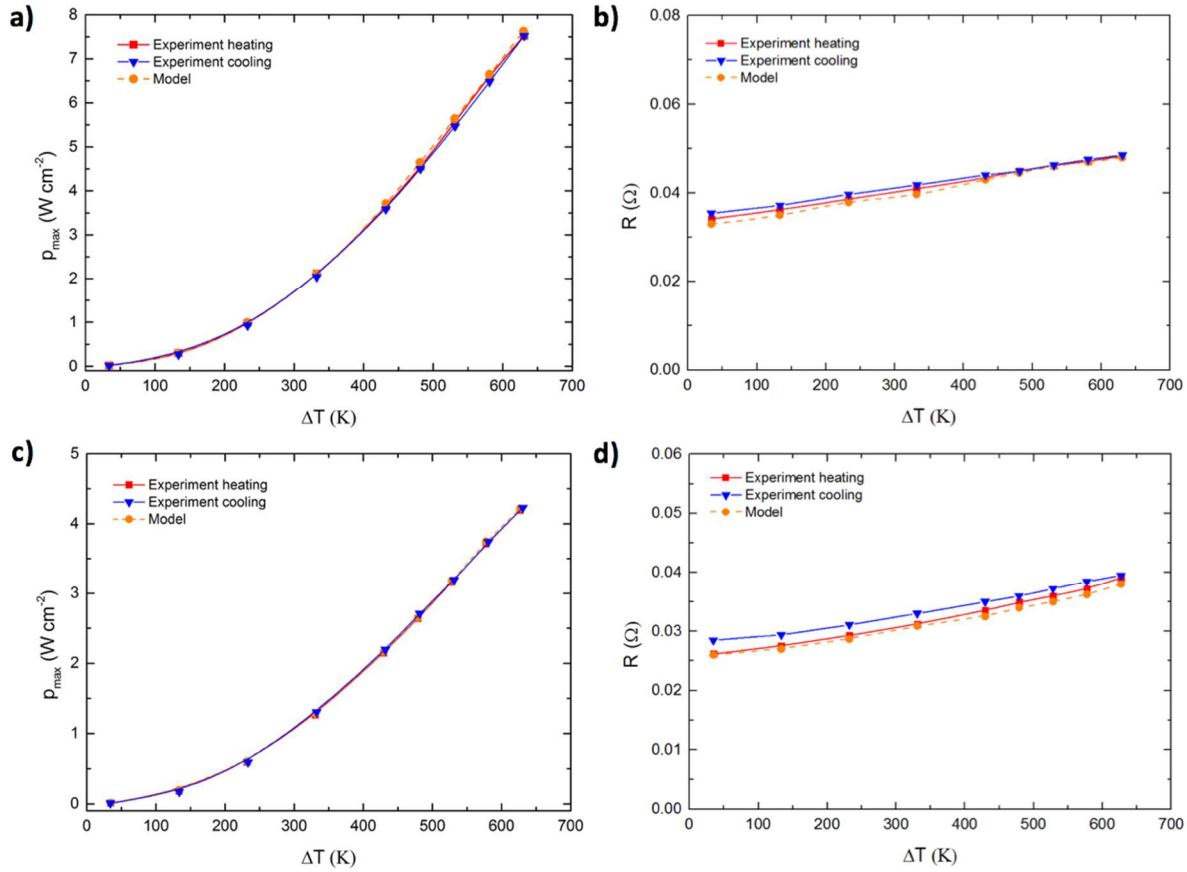

Figure S14. Comparison between measurements and theoretical predictions for the skutterudite-based TEG with $(Ti/Ag)_{n,p}$ metallic composites. The maximum output power P_{max} and internal resistance R of the module are compared as a function of the applied temperature difference for two modules with skutterudite height of (**a**, **b**) 1 mm and (**c**, **d**) 0.5 mm. For both modules, the measurements have been performed upon heating and cooling. The excellent agreement observed between theory and experiments highlights the good control of the electrical contact resistance at the interfaces achieved in the fabrication process of the *p*- and *n*-type legs.